Distinguishing Modified Newtonian Dynamics from Dark Matter with Galaxy-galaxy Lensing Measurements

by

Lanlan Tian

A Thesis Submitted in Partial Fulfillment of the
Requirements for the Degree of

Master of Science

in the Department of Physics and Astronomy

University of Victoria

Distinguishing Modified Newtonian Dynamics from Dark Matter with Galaxy-galaxy Lensing Measurements

by

Lanlan Tian

Supervisory Committee

Dr. Henk Hoekstra, Supervisor (Department of Physics and Astronomy)

Dr. Sara Ellison, Member (Department of Physics and Astronomy)

Dr. Jon Willis, Member (Department of Physics and Astronomy)

Supervisory Committee

Dr. Henk Hoekstra, Supervisor (Department of Physics and Astronomy)

Dr. Sara Ellison, Member (Department of Physics and Astronomy)

Dr. Jon Willis, Member (Department of Physics and Astronomy)

Abstract

As an alternative to dark matter, Modified Newtonian Dynamics (MOND) can explain dynamical measurements of galaxies on small scales. It is, however, unclear whether MOND still works for galaxies on the large scale. In this study, we use galaxy-galaxy (g-g) weak lensing measurements to examine MOND in the outer regions of galaxies. First, we study the amplitude of the weak gravitational lensing signal as a function of stellar mass around relatively isolated galaxies. We find that our measurements are inconsistent with the predictions from MOND. Second, we examine whether MOND can produce an anisotropic lensing signal as observed in the real data. Starting with a mass distribution of an extremely high ellipticity, we find it is very hard for MOND to reproduce the observed extensive anisotropic lensing signal from only the visible mass. Because the g-g lensing is measured at radii of up to hundreds of kiloparsecs, these two tests indicate that MOND does not work in outer regions of galaxies. Our study casts serious doubt on the notation that MOND can convincingly prove itself as a viable alternative to dark matter.

Table of Contents

List of Figures

Acknowledgements

First I want to thank my supervisor Dr. Henk Hoekstra. It has been an honor to be his first full-time graduate student. He has taught me how quality astronomical research is done. I appreciate all the time, ideas, and funding he has contributed, which made my experience at the University of Victoria (UVIC) stimulating. The joy and enthusiasm he has for his research was motivational for me. I am also thankful for the excellent role model of a successful astronomer that he has been for me.

I am grateful to my committee member Dr. Sara Ellison, who helped me to begin my study at UVIC. I also thank my other committee member: Dr. Jon Willis. His invaluable feedback has helped me to improve this thesis greatly.

I would also like to thank Lisa Glass for her generous help in many ways. Because of her, although living alone in Canada as an international student, I felt warmly encouraged, especially when I encountered various difficulties. I would like to extend my appreciation to Chris Bildfell for his kind help with my work. I am also grateful to my friends, the astronomy graduate students and postdocs at UVIC who have contributed to my personal and professional time in Victoria: Mego Wang, Rachel Friesen, Helen Kirk, Eric Hsiao, Wesley Fraser, Melissa Graham, Karun Thanjavur, Aida Ghazvini Zadeh, Aaron Ludlow and Andisheh Mahdavi. The staff in the Physics and Astronomy office (Rosemary Barlow, Joy Austin, Chantal Laliberté, Milena Hoekstra and Susan Gnucci) as well as Stephenson Yang, who provided many hours of computer supports, are also much appreciated.

Last but not least, I thank my parents for spiritually supporting me through all these years. Although they do not fully understand what astronomy is, they know astronomy is my dream. I thank my brother and sister-in-law for always being there

for my parents and for taking care of them so that I do not need to worry too much about them when I am far away from them. Finally, I would like to express immense gratitude to my beloved husband Jiren Liu, who gives me the most important support of my work and life. Without him, my study at UVIC would not have been possible.

Dedication

This thesis is dedicated to my beloved father.

"How does it happen that a properly endowed natural scientist comes to concern himself with epistemology? Is there no more valuable work in his specialty? I hear many of my colleagues saying, and I sense it from many more, that they feel this way. I cannot share this sentiment. ...Concepts that have proven useful in ordering things easily achieve such an authority over us that we forget their earthly origins and accept them as unalterable givens. Thus they come to be stamped as 'necessities of thought', 'a priori givens', etc. The path of scientific advance is often made impassable for a long time through such errors. For that reason, it is by no means an idle game if we become practiced in analyzing the long common place concepts and exhibiting those circumstances upon which their justification and usefulness depend, how they have grown up, individually, out of the givens of experience. By this means, their all-too-great authority will be broken." –Einstein

Chapter 1

Introduction

A remarkable feature of modern cosmology is that we have a theoretical framework which can make predictions and its predictions can be tested by observations. General relativity (GR) discovered by Einstein in the last century provides the basis of our model of the universe. Today, after almost one hundred years, we have collected an enormous amount of observations of the universe. These data cover observations ranging from the early universe (e.g., cosmic microwave background observations), the large-scale structure of the present universe (e.g., the Sloan Digital Sky Survey, the 2 degree Field Galaxy Redshift Survey) and the expansion of the universe (e.g., supernovae observations of the accelerating expansion of the universe). Based on GR, a cosmology model called Lambda Cold Dark Matter (ΛCDM) has been developed in which the universe is dominated by cold dark matter and a cosmological constant Λ. The cosmological constant Λ can be generalized to 'dark energy' to account for the current accelerating expansion of the universe. Cold dark matter is conceived as non-baryonic matter which is cold (i.e., its velocity is non-relativistic ($v \ll c$) at the epoch of radiation-matter equality), and interacts with itself and other particles through gravity only. This model is well-developed and widely applied to galactic and cosmological observations. It fits a range of observations extremely well, most notably the cosmic background radiation (Spergel et al. 2007).

The need for dark matter to explain astronomical observations has been a long-standing issue and a number of dark matter candidates, inspired by particle physics, have been suggested. The current lack of a direct detection of the dark matter particle has led to the desire for an alternative approach to explain the observations. Instead of invoking dark matter, proponents of alternative theories to dark matter assume that the laws of gravity differ from Newtonian gravity on scales where gravity is weak, which cannot yet be reproduced in current gravitational experiments. One of the most studied alternatives is Modified Newtonian Dynamics (MOND) proposed by Milgrom (1983b). It has evolved over the past 25 years from an empirical fit to galaxy rotation curve data (Milgrom 1983a; Sanders and McGaugh 2002) to a relativistic tensor-vector-scalar theory (TeVeS, Bekenstein 2004). Recent developments include a theory of a vector field with a non-linear coupling to the space-time metric (Zlosnik et al. 2007; Zhao 2007).

MOND works particularly well on galactic dynamics (for a review, see Sanders and McGaugh (2002)). Dynamical measurements, however, explore gravitational potentials in inner regions of galaxies only, due to using visible matter (stars or gas) as their tracers. Given the situation that a dark matter particle has not yet been detected in the lab and that MOND works well in galaxies on small scales, it is interesting to ask whether or not MOND is consistent with observations from outer regions of galaxies.

This thesis presents a study to test MOND in outer regions of galaxies. We use galaxy-galaxy (g-g) lensing measurements to explore the gravitational potentials of galaxies at large radii.

First of all, we review the observational evidence of the mass discrepancy which requires invoking dark matter, MOND, or other alternative theories of gravity.

1.1 Observational evidence for the mass discrepancy

As early as 1933, astrophysicist Fritz Zwicky studied the radial velocities of galaxies in the Coma cluster and found that the required mass of the cluster to explain the high velocity dispersion (≈ 1000 km/s) of the member galaxies was about 400 times larger than the estimated visible mass (Zwicky 1937). The required mass was deduced by applying the virial theorem in Newtonian Dynamics. Zwicky's discovery indicates that for clusters of galaxies, the most massive gravitationally-bound systems, there is a big discrepancy between the required Newtonian gravitational mass and its visible mass.

Approximately 40 years after Zwicky's observations, the evidence for a mass discrepancy was also found within galaxies. The pioneering work was done by Vera Rubin and Kent Ford. In the late 1960s, they studied circular velocities of the spiral galaxy M31 (Andromeda) using spectroscopic observations of HII clouds (Rubin and Ford 1970). They found the circular velocities were nearby a constant at large radii (up to ~ 24 kpc). This is in striking contrast to the prediction of Keplerian motion. With the assumption that the visible mass (stars and HII clouds) were the primary mass of the galaxy, it predicts that the circular velocity should decrease with radius. Further, Rubin and her collaborators observed another 54 spiral galaxies and confirmed that flat rotation curves are a general phenomenon in spiral galaxies (Rubin et al. 1985).

Together with Rubin's findings for spiral galaxies and Zwicky's work on galaxy clusters, the observational evidence for a mass discrepancy has increased over several decades. These observations not only include more measurements of rotation velocities in spiral galaxies and velocity dispersions in galaxy clusters (Smith 1936; Kahn and Woltjer 1959; van den Bergh 1961; Sarazin 1988; Alonso et al. 1999; Blindert et al. 2004; Goto 2005), but also include measurements of hot gas in elliptical galax-

ies and galaxy clusters (Lewis et al. 2003) and the gravitational lensing by galaxies and galaxy clusters (Grossman and Narayan 1989; Bergmann et al. 1990; Pello et al. 1991; Kneib et al. 1993; Mellier et al. 1993; Fahlman et al. 1994; Kaiser 1995; Tyson and Fischer 1995; Smail et al. 1995; Squires et al. 1996; Seitz and Schneider 1996; Luppino and Kaiser 1997). All these observations consistently indicate that the mass required to account for the observables is much more than the amount of visible matter (stars and gas). Such a mass discrepancy occurs on a variety of mass scales, from dwarf galaxies to rich galaxy clusters.

To quantify the mass discrepancy, one convenient quantity is the mass-to-light ratio (M/L). The mass M is the Newtonian gravitational mass, which is deduced with different methods, including circular velocity, velocity dispersion, gravitational lensing and X-ray gas temperature. Light or luminosity (L), as a direct observable, is intrinsically associated with the visible mass. Therefore, the ratio of the deduced mass to luminosity can reflect the mass discrepancy between Newtonian gravitational mass and the visible mass. The larger the value of M/L, the bigger the mass discrepancy.

In the following, I will demonstrate the typical observational evidence for this mass discrepancy.

1.1.1 Galactic rotation curves

In galaxies, the most impressive evidence for the mass discrepancy comes from rotation curves. A rotation curve is the plot of the circular velocity v_c as a function of distance r from the center of the galaxy. The velocity is typically measured from motions of stars or HII clouds. To date, thousands of rotation curves have been measured. This kind of measurement can reach a range of up to ~ 30 kpc from the center of the galaxy. These rotation curves do not decrease as expected but instead are flat – outside of the central bulge the speed is nearly a constant function of radius (the solid line in Fig.1.1). Consider a star or gas cloud in circular orbit at radius r.

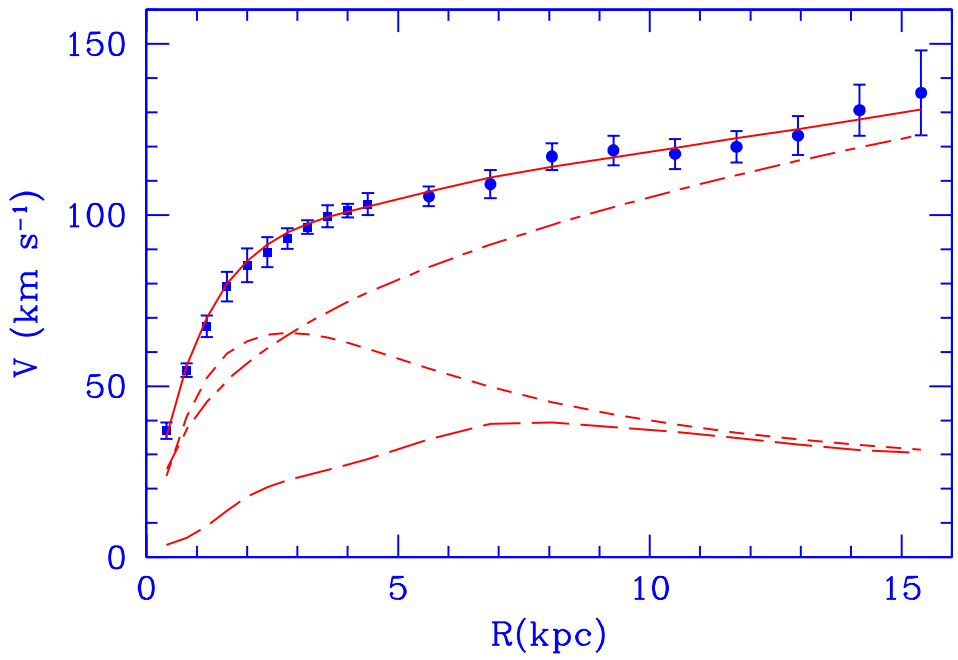

Figure 1.1: M33 rotation curve (points) compared with the best-fitting model (continuous line). Also shown are the halo contribution (dot-dashed line), the stellar disc (short-dashed line) and the gas contribution (long-dashed line) (Corbelli et al. 2000).

The acceleration of gravity must be balanced by the centrifugal acceleration:

$$\frac{GM(<r)}{r^2} = \frac{v_c^2(r)}{r} => M(<r) = \frac{rv_c^2(r)}{G} \tag{1.1}$$

where $M(<r)$ is the Newtonian gravitational mass enclosed inside radius r, and G is the gravitational constant. Once the rotation velocity is obtained, we can derive the necessary Newtonian gravitational mass M by applying Eq.(1.1). A flat rotation curve implies that the mass increases linearly with the radius. Mass models that consider only the visible mass in the available photometric data (stellar matter and visible gas) do not provide flat rotation curves. To reconcile the observations requires a large halo contribution from non-luminous matter (see the dot-dashed line in Fig.1.1). The study of rotation curves imply that, for spiral galaxies including our own, the mass-to-light ratio is $\sim 40 M_\odot/L_\odot$, which is ten times greater than that of

the stars ($\sim 4M_\odot/L_\odot$) in the galaxy (Ryden 2003).

1.1.2 Velocity Dispersions in Galaxy Clusters

Another piece of dynamical evidence comes from measurements of velocity dispersions in galaxy clusters. As mentioned previously, this measurement in the Coma cluster by Zwicky provided the first evidence for the mass discrepancy. Since Zwicky's work in the 1930s, there have been many kinematic studies of other clusters (Smith 1936; Kahn and Woltjer 1959; van den Bergh 1961; Alonso et al. 1999; Blindert et al. 2004; Goto 2005). The radial velocity dispersions of galaxies σ_v can be associated with the cluster's gravitational mass M by the virial theorem. Under the Newtonian dynamical framework, this mass is approximated by (Carroll and Ostlie 1996)

$$M \approx \frac{5\sigma_v^2 R}{G}, \tag{1.2}$$

where R is the size of the cluster. In the case of the Coma cluster, $\sigma_v = 10^3$ km/s. With the cluster radius $R = 3$Mpc, Eq.(1.2) leads to a mass of $M \approx 10^{15} M_\odot$. Since the visible luminosity of the Coma cluster is about $5 \times 10^{12} L_\odot$, the mass-to-light ratio of the cluster is $200 - 300 M_\odot/L_\odot$ (Sarazin 1988). This example indicates the mass discrepancy in galaxy clusters is much larger than that in galaxies.

1.1.3 X-ray Imaging

Our understanding of galaxy clusters has been greatly improved by studying their X-ray emission. It is well known that most of the visible matter in clusters of galaxies is in the form of excited, hot gas (Ryden 2003). This gas has a temperature of 10-100 million Kelvin and radiates X-rays via free-free emission. Under the condition of hydrostatic equilibrium and the assumption of an ideal gas, the Newtonian gravitational mass of the cluster within a radius r can be associated with its temperature T

and density $\rho_g(r)$:

$$M(<r) = -\frac{kTr}{Gm_{gas}}(\frac{dln\rho_g}{dlnr} + \frac{dlnT}{dlnr}), \tag{1.3}$$

where k is the Boltzmann constant, m_{gas} is the mean mass of a gas particle. The temperature T of the X-ray gas can be obtained from the observed X-ray spectrum. And the gas density $\rho_g(r)$ can be modeled with an isothermal β model:

$$\rho_g(r) = \rho_g(0)(1 + (\frac{r}{r_c})^2)^{-3\beta/2}, \tag{1.4}$$

where r_c is the core radius. The X-ray analysis by Lewis et al. (2003) shows that the M/L ratio resulting from this method agrees on average with that from dynamical analysis discussed in 1.1.2.

1.1.4 Gravitational Lensing

The mass discrepancies found in galaxies and galaxy clusters from dynamical studies and X-ray imaging have been further confirmed by observations of gravitational lensing (GL). Gravitational lensing refers to the phenomena predicted by GR in which the light from background objects is deflected by the mass of foreground objects. There are two classes of GL, strong lensing and weak lensing, depending on the magnitude of the deflection. The procedure to derive the Newtonian gravitational mass from GL is discussed in detail in Chapter 2.

Strong lensing by galaxy clusters results in multiple images. The studies of these systems indicate very large Newtonian gravitational masses for lensing systems. The values of M/L from strong lensing measurements are $240h - 500hM_\odot/L_\odot$ (Grossman and Narayan 1989; Bergmann et al. 1990; Pello et al. 1991; Kneib et al. 1993; Mellier et al. 1993). Because strong lensing occurs near the lenses on the sky, the masses derived from this kind of measurement are limited to relatively small regions. For massive galaxies ($\sim 10^{12} - 10^{13}M_\odot$), this distance is of order 10 kpc; for galaxy

clusters, this distance is of order 100 kpc. To explore the mass over large radii, weak lensing is applied. Weak lensing refers to phenomena in which the gravitational field of the foreground object introduces small coherent distortions in the images of distant background objects. As shown by Kaiser and Squires (1993), it can be used to reconstruct foreground mass distributions from the distorted images of background galaxies. This technique and its variants have been applied to a number of galaxies and clusters (Fahlman et al. 1994; Kaiser 1995; Tyson and Fischer 1995; Smail et al. 1995; Squires et al. 1996; Seitz and Schneider 1996; Luppino and Kaiser 1997). The mass-to-light ratios inferred from weak lensing by clusters are generally even higher than that from strong lensing, $400h - 800hM_{\odot}/L_{\odot}$.

1.1.5 Summary

All of these observations indicate that the derived Newtonian gravitational mass-to-light ratio in galaxies and clusters is generally large. Fig.1.2 summarises the results (Bahcall et al. 2000). To explain the mass discrepancies observed across different mass-scale systems, two fundamental different solutions have been proposed: dark matter and modified gravity theories.

1.2 Solution: Dark Matter Scenario

Zwicky's observations of the mass discrepancy in the Coma cluster led him to propose a non-visible mass component called dark matter (DM). The idea of dark matter has been studied for more than 70 years. The dark matter scenario has become the most popular one to explain the observations.

The strength of the DM scenario is not only that it can explain the problem of mass discrepancy, but also it helps to explain other important problems. The study of the stability of disk galaxies shows that a massive dark matter halo is needed to keep the disk structure stable (Ostriker and Peebles 1973). Besides, the most compelling support for dark matter comes from cosmological studies. For example, research

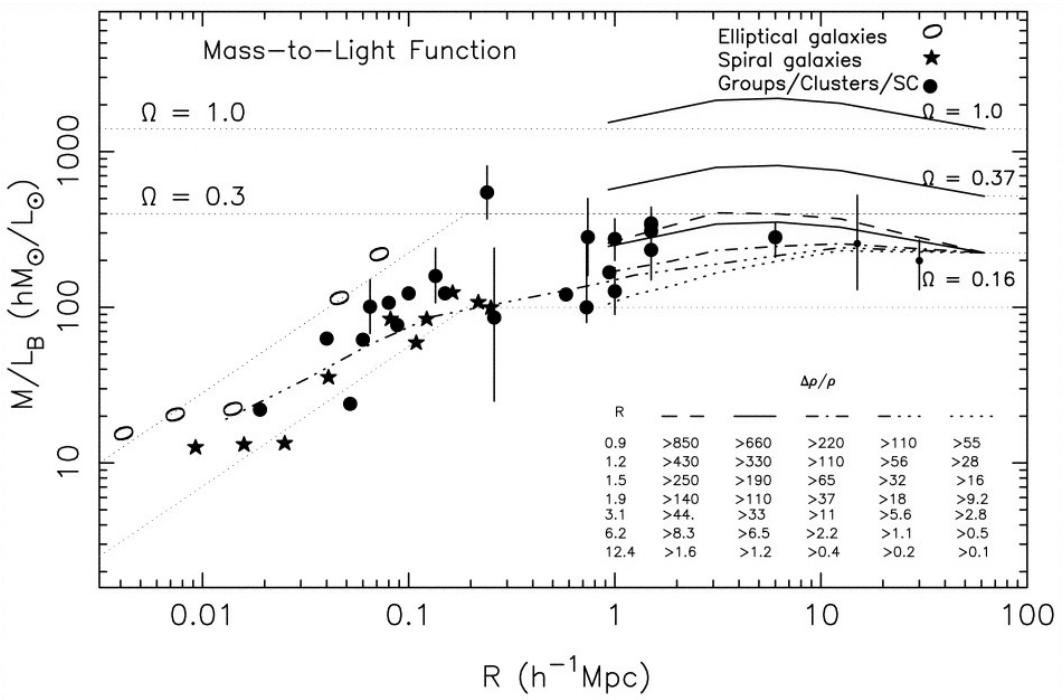

Figure 1.2: Mass-to-light ratios on different scales. The data points include galaxies (spirals and ellipticals, as indicated by the different symbols), groups, rich clusters (at $R = 1.5h^{-1}Mpc$), supercluster (MS 0302 at $\sim 6h^{-1}Mpc$, from weak-lensing observations). The curves come from the simulation results. (Bahcall et al. 2000)

on the large-scale structure of the universe reveals that without DM, it is difficult to explain how the universe grows from the initial baryonic density perturbation ($\sim 10^{-5}$) to highly clustered structure seen today.

A cosmological model involving dark matter called the ΛCDM model has become a very successful model. It has consistently passed many observational tests. In particular, it successfully explains the shape of the power spectrum of the cosmic microwave background (CMB) radiation. This model, however, has some unsolved problems. For example, numerical simulations of ΛCDM predict cuspy dark matter halos in dwarf galaxies, which are not supported by observations (Navarro et al. 1996; Moore et al. 1999). This is referred to as the 'core' or 'cusp' problem. Another intriguing problem for DM is that no corresponding dark matter particles have been detected in the lab so far. This has led some people to look for alternatives to DM.

1.3 Alternative Solution: MOND

As an alternative to DM, Modified Newtonian Dynamics was proposed by Mordehai Milgrom in 1983 (Milgrom 1983b). Motivated by fitting the flat galactic rotation curve, Milgrom proposed that, instead of the existence of dark matter, gravity becomes stronger in the Newtonian weak field limit.That is, the real gravitational acceleration goes as $g = \sqrt{g_N a_0}$ when $g < a_0$, where $a_0 \approx 1.2 \times 10^{-8}\ ms^{-2}$ is a characteristic acceleration and g_N is the Newtonian gravitational acceleration. Based on this modification, the constant circular velocity in spiral galaxies can be derived.

As an empirical theory, MOND succeeds in explaining galactic rotation curves (Sanders and McGaugh 2002). This success in dwarf galaxies is particularly remarkable, given that ΛCMD predictions fail in those galaxies (the 'cusp' problem in dwarf galaxies; refer to section 1.2). Besides its success in the explanation of rotation curves, MOND also naturally predicts the Tully-Fisher relation (Tully & Fisher 1977). The Tully-Fisher relation is an empirical relationship between the intrinsic

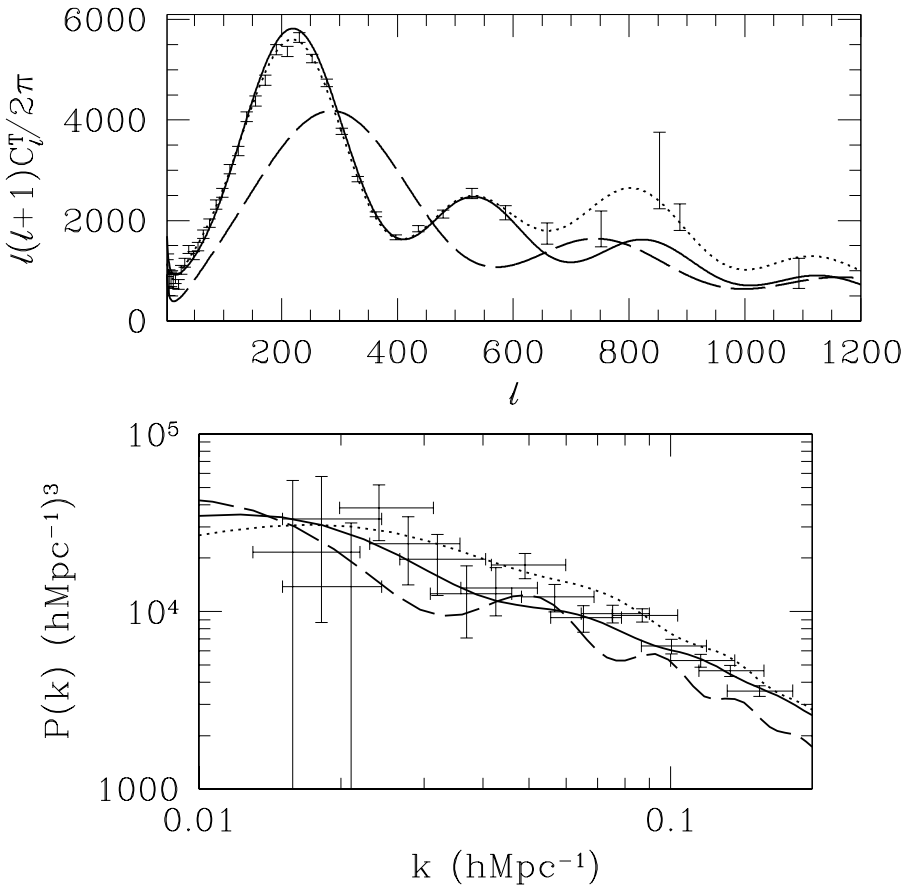

Figure 1.3: The angular power spectrum of the CMB (top panel) and the power spectrum of the baryon density (bottom panel) for a MOND universe (with $a_0 \simeq 4.2 \times 10^{-8} cm/s^2$) with $\Omega_\Lambda = 0.78$ and $\Omega_\nu = 0.17$ and $\Omega_B = 0.05$ (solid line), for a MOND universe $\Omega_\Lambda = 0.95$ and $\Omega_B = 0.05$ (dashed line) and for the Λ-CDM model (dotted line). A collection of data points from CMB experiments and Sloan are overplotted.(Skordis et al. 2006)

luminosity (proportional to the stellar mass) of a spiral galaxy and its maximum rotation velocity.

The success of MOND on galactic scales is impressive. It encourages people to extend its application to more observations. In 2004, Bekenstein (2004) gave MOND a relativistic form TeVeS. This work is a fundamentally big step for MOND. It allows MOND to escape from the realm of purely empirical theories and become a serious physical theory, extending applications of MOND to fields where it could not be applied before. For example, we can now use MOND in the analysis of gravitational lensing. Using TeVeS and massive neutrinos, some authors have even worked out a cosmological model, which predicts the first two peaks of CMB power spectrum equally as well as the ΛCDM model (see Fig.1.3) (Skordis et al. 2006).

MOND, however, meets some trouble when it is applied to galaxy clusters. In MOND, there is still a factor of 1.5-4 discrepancy between the binding mass and the baryonic mass in clusters. Sanders (2003) proposed a massive neutrino to eliminate this gap. However, the studies of dynamics of cool clusters (Pointecouteau and Silk 2005) and weak lensing by clusters (Takahashi and Chiba 2007) report the required neutrino mass is too high to be allowed by particle physics. Also CMB observations by the Wilkinson Microwave Anisotropy Probe (WMAP) reports that the TeVeS prediction of the third peak of CMB power spectrum is lower than what is observed (Spergel et al. 2007). In short, compared with ΛCDM, MOND is far from a consistent cosmological model.

1.4 Distinguishing MOND from DM

During its 25 years of development, MOND has become a very compelling theory to challenge the DM scenario. It is able to reproduce many observations with accuracy comparable to DM theories. In the dwarf galaxies and Low Surface Brightness (LSB) galaxies, it seems MOND works even better than DM theories (Angus 2008). From

this point, it's very interesting to investigate this theory further.

Since MOND's power has been recognized in the 1990s, people have started to design all kinds of tests to distinguish MOND from DM. The previous discrimination work ranges from kinematics in the local universe to cosmological observations.

Most tests have focussed on galactic scales, where MOND works particularly well (e.g. Read & Moore 2005, Famaey et al 2006, Nipoti et al 2007, Corbelli & Salucci 2006, Gentile et al. 2007, Zhao & Famaey 2006, Famaey & Binney 2005). There are also a few tests on sub-galactic scales using velocity dispersion of globular clusters (eg. Baumgardt et al. 2005). These tests have not found a definite discrimination between MOND and Newtonian DM. Some authors also attempt to work out where MOND predictions differ unambiguously from ΛCDM on sub-galactic scales to cosmological scales. For example, Hongsheng Zhao figured out that there would be a different shape for Roche lobes in binary systems under MOND (Zhao 2005; Zhao and Tian 2006). Mortlock and Turner proposed to detect cosmological microlensing which is expected to have different signals for MOND and ΛDCM (Mortlock and Turner 2001b). Unfortunately, these tests will have to wait for future surveys because they are outside the capabilities of current facitities.

1.5 Outline of the thesis

In this study, we seek to use weak lensing by galaxies to distinguish MOND from dark matter. Different from previous work, we focus on testing MOND in the outer regions of galaxies. This is because in these regions MOND and ΛCDM would differ most markedly. These regions in the dark matter paradigm are called 'dark matter dominated' and in MOND are called 'deep-MOND regions'. Due to lack of visible tracers, the potential of a galaxy in those regions is seldom explored. Although the study of kinematics of satellite galaxies provides an available approach, the problem of whether the virialization assumption is valid in the system puts doubts on the

corresponding results. Weak lensing provides an ideal tool to investigate this. The theory of gravitational lensing in the context of MOND is discussed in Chapter 2. Thanks to the development of measurement and analysis techniques, sufficiently accurate weak lensing data can be obtained in the largest surveys (e.g., the Sloan Digital Sky Survey, the Red-Sequence Cluster Survey). With weak lensing measurement, the gravitational potential can be explored out to a radius of hundreds of kiloparsecs.

In our first test, considering MOND as a non-linear gravity theory, compared to GR, there should be fundamental differences in their global scaling relations (e.g. the lensing signal versus the luminosity). Rather than comparing the strength of the gravitational potential, we focus on how it changes with baryonic mass. This test will be addressed in detail in Chapter 3.

In the MOND paradigm, only luminous mass, or more accurately baryonic mass, accounts for all the astronomical observations. We can test MOND by examining whether mass follows the light distribution. Since the azimuthal lensing signal follows the gravitational field shape (ie. mass distribution), we can compare the level of anisotropy of the galaxy-galaxy (g-g) lensing signal with that of the light distribution. Mortlock and Turner (2001a,b) proposed to test MOND by examining the deviation from azimuthal symmetry in the shear signal with galaxy-galaxy lensing. When Mortlock and Turner proposed this test, the g-g lensing data were not good enough. Now after a few years, with the great improvement of weak lensing measurements, significantly anisotropic lensing signals have been detected (Hoekstra et al. 2004; Parker et al. 2007; Mandelbaum et al. 2006a). With those data, we can now preform this test as our second one in Chapter 4. We present our conclusions in Chapter 5.

Throughout this thesis, we adopt a Hubble parameter $H_0 = 70$ km/s/Mpc and all the error bars correspond to 68% confidence limits (1σ).

Chapter 2

Galaxy-galaxy lensing

In this chapter, we will address the observational method we use in our tests of MOND: galaxy-galaxy (g-g) lensing. The gravitational field of a foreground galaxy introduces small coherent distortions in the images of distant background galaxies. The distortion induced by an individual galaxy is too small to be detected. The ensemble-averaged signal (distortion) around galaxies, however, can be detected in current large imaging surveys. This phenomena is known as g-g lensing.

The g-g lensing signal which we quantify by the tangential shear γ_t, can be obtained from the measurements of the shapes of background galaxies. Due to the telescope and atmosphere i.e. seeing, the observed shapes of galaxies are changed by the point spread function (PSF). The shapes of galaxies are made rounder by seeing and the intrinsic size of the PSF. Also, PSF anisotropy introduces alignments in the shapes of galaxies, which can cause a false lensing signal. To measure the true g-g lensing signal, the shapes of galaxies need to be corrected. This PSF correction is the most important step in any weak lensing analysis. Once the unbiased shapes are measured, the average ellipticity of background galaxies at a given angular distance is used to obtain the tangential shear (Bartelmann and Schneider 2001; Hoekstra and Jain 2008).

Galaxy-galaxy lensing has unique advantage for studying the gravitational po-

tential around galaxies. It can probe the potential on large scales (hundreds of kpc) without any assumptions about the dynamical state of the lens galaxies. In comparison, the studies from the measurements of motions of stars or gas and strong lensing only probe the gravitational potential on small scales because of the lack of visible tracers at large radii. Although the studies of satellite galaxies or gas halos provide some information about the potential on large scales, the assumptions in the analysis set limits on the accuracy of the results. Because of this unique advantage of g-g lensing, we can apply it to test MOND on large scales.

In this chapter, we first introduce the basic concept of gravitational lensing in §2.1. In §2.2, §2.3, we describe how to calculate g-g lensing signal in GR and MOND, respectively. In §2.4, we discuss how different density profiles of a galaxy affect the lensing signal. The answer to this problem turns out to be a very useful property for further study.

2.1 Basic Concepts in Gravitational Lensing

In this part, we briefly describe the basic concepts in GL. For detailed lectures on GL, please refer to Narayan and Bartelmann (1996). The geometry of a general gravitational lens system is shown in Fig. 2.1. A light ray from a source S is deflected by an angle $\hat{\alpha}$ at the lens and reaches an observer O. The positions of the source S and the image I are related through the equation:

$$\boldsymbol{\beta} = \boldsymbol{\theta} - \boldsymbol{\alpha}(\boldsymbol{\theta}) \ . \tag{2.1}$$

Equation (2.1) is the called lens equation. The angle $\boldsymbol{\alpha}$ is called the deflection angle. In the circular-symmetric case the deflection angle is given by

$$\alpha(\xi) = \frac{4GM(\xi)}{c^2}\frac{1}{\xi} \tag{2.2}$$

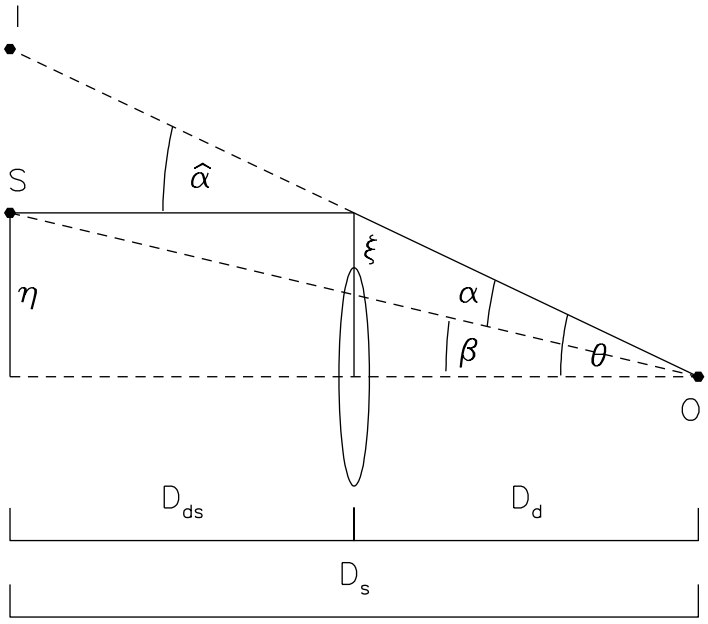

Figure 2.1: Illustration of a gravitational lens system. Figure from Narayan and Bartelmann (1996).

where $M(\xi)$ is the mass inside a radius ξ. For a point lens of mass M, the lens equation becomes:

$$\beta(\theta) = \theta - \frac{4GM(\xi)}{c^2}\frac{1}{\theta} \, . \tag{2.3}$$

When the source lies exactly behind the lens (ie. $\beta = 0$), due to the symmetry, a ring-like image occurs whose angular radius is called the Einstein radius:

$$\theta_E = \sqrt{\frac{4GM}{c^2}\frac{D_{ls}}{D_l D_s}} \, . \tag{2.4}$$

where D_s, D_l are the distance from the observer to the source and lens, respectively; D_{ls} is the distance between the source and the lens.

Given an extended distribution of matter, the lensing potential $\psi(\boldsymbol{\theta})$ is defined as the projected 3-D Newtonian gravitational potential Φ on the lens plane:

$$\psi(\boldsymbol{\theta}) = \frac{2D_{ls}}{D_l D_s c^2}\int_{-\infty}^{+\infty} \Phi(D_{\mathrm{d}}\boldsymbol{\theta}, z)\, dz \, . \tag{2.5}$$

The lensing potential has two important properties:

(1) The gradient of $\psi(\boldsymbol{\theta})$ gives the deflection angle:

$$\boldsymbol{\nabla}_\theta \psi = \boldsymbol{\alpha} \, , \tag{2.6}$$

(2) Define convergence $\kappa(\boldsymbol{\theta})$ as the surface mass density scaled with its critical value Σ_{cr}, i.e.:

$$\kappa(\boldsymbol{\theta}) = \frac{\Sigma(\theta)}{\Sigma_{cr}}, \Sigma_{cr} = \frac{c^2}{4\pi G}\frac{D_s}{D_l D_{ls}} \tag{2.7}$$

such that the surface density $\Sigma(r)$ is

$$\Sigma(r) = \int_{-\infty}^{+\infty} \rho(R)\, dz, R = \sqrt{r^2 + z^2}, r = \sqrt{x^2 + y^2}; \tag{2.8}$$

then there is a relation between the convergence κ and the lensing potential ψ:

$$\nabla^2_\theta \psi \equiv 2\kappa(\boldsymbol{\theta}) \ . \tag{2.9}$$

One of the main features of gravitational lensing is the distortion which it introduces into the shape of the sources. The distortion arises because light rays are deflected differentially. The distortion of images can be described by the Jacobian matrix $\mathcal{A}$,

$$\mathcal{A} \equiv \frac{\partial \boldsymbol{\beta}}{\partial \boldsymbol{\theta}} = \left(\delta_{ij} - \frac{\partial \alpha_i(\boldsymbol{\theta})}{\partial \theta_j} \right) = \left(\delta_{ij} - \frac{\partial^2 \psi(\boldsymbol{\theta})}{\partial \theta_i \partial \theta_j} \right) \ . \tag{2.10}$$

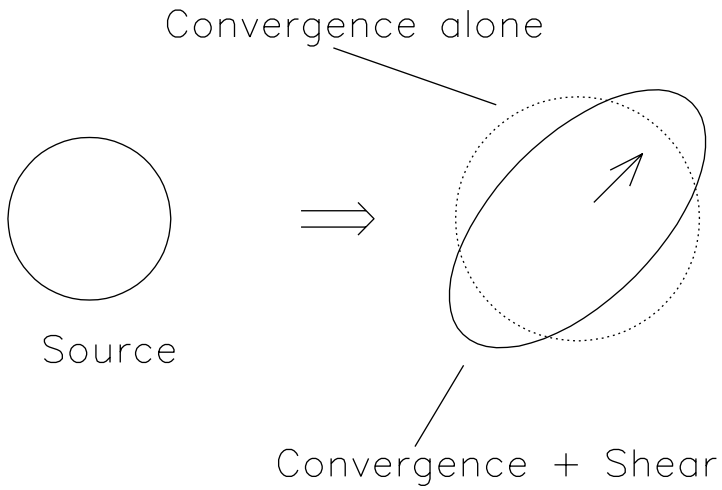

Figure 2.2: Distortion effects due to convergence and shear on a circular source. Figure from Narayan and Bartelmann (1996).

For convenience, we introduce the abbreviation

$$\frac{\partial^2 \psi}{\partial \theta_i \partial \theta_j} \equiv \psi_{ij} \ . \tag{2.11}$$

Define the components of the *shear* tensor,

$$\begin{aligned} \gamma_1(\boldsymbol{\theta}) &= \frac{1}{2}\left(\psi_{11} - \psi_{22}\right) \equiv \gamma(\boldsymbol{\theta}) \cos\left[2\phi(\boldsymbol{\theta})\right] \ , \\ \gamma_2(\boldsymbol{\theta}) &= \psi_{12} = \psi_{21} \equiv \gamma(\boldsymbol{\theta}) \sin\left[2\phi(\boldsymbol{\theta})\right] \ . \end{aligned} \tag{2.12}$$

With these definitions, the Jacobian matrix can be written

$$\begin{aligned} \mathcal{A} &= \begin{pmatrix} 1 - \kappa - \gamma_1 & -\gamma_2 \\ -\gamma_2 & 1 - \kappa + \gamma_1 \end{pmatrix} \\ &= (1 - \kappa) \begin{pmatrix} 1 & 0 \\ 0 & 1 \end{pmatrix} - \gamma \begin{pmatrix} \cos 2\phi & \sin 2\phi \\ \sin 2\phi & -\cos 2\phi \end{pmatrix} \ . \end{aligned} \tag{2.13}$$

Equation 2.13 above demonstrates the meaning of both convergence and shear. Convergence cause an isotropic magnification of a source. The source is mapped onto an image with the same shape but different size. Shear introduces anisotropy into the lens mapping. The quantity $\gamma = (\gamma_1^2 + \gamma_2^2)^{1/2}$ describes the magnitude of the shear and ϕ describes its orientation. Fig. 2.1 shows with non-zero κ and γ how a circular source becomes an elliptical image.

2.2 Calculating Weak Lensing Signal in GR

The amplitude of the distortion induced by one galaxy can be measured by the intensity of the shear γ. The shear tends to be tangential to the lens isodensity contours, called tangential shear γ_t. In GR, γ_t is closely associated with the mass density of the galaxy. In axially symmetric cases (for example, a spherical distribution), given

the radial density profile of the galaxy $\rho(R)$, there is

$$\gamma_t(r) = \bar{\kappa}(< r) - \kappa(r), \tag{2.14}$$

where κ, convergence, is the rescaled surface density and $\bar{\kappa}(< r)$ is the mean convergence within the radius r.

In the context of GR, the galaxy-galaxy lensing signal within ~ 400 kpc is well described by a Singular Isothermal Sphere (SIS) model (Hoekstra et al. 2004) by

$$\rho(r) = \frac{\sigma_v^2}{2\pi G r^2},$$

where σ_v is the line-of-sight velocity dispersion. The corresponding azimuthally averaged tangential shear (which corresponds to the observed g-g lensing signal) is given by

$$\langle \gamma_t \rangle(r) = \kappa(r) = \frac{r_E}{2r}, \tag{2.15}$$

where r_E is the Einstein radius, which is related to σ_v through

$$r_E = 4\pi \left(\frac{\sigma_v}{c}\right)^2 \frac{D_{ls}}{D_s}. \tag{2.16}$$

2.3 Calculating a Weak Lensing Signal in MOND

Since Bekenstein (2004) published a relativistic form of MOND known as Tensor-Vector-Scalar gravity, MOND can be applied to a gravitational lensing field. The procedures to calculate the lensing quantities in TeVeS are similar to those in GR (Zhao 2006). The difference between these is that the gravitational potentials that are used are different. In GR, the potential is the Newtonian gravitational potential. In TeVeS, it is the MOND gravitational potential.

2.3.1 Calculating the MOND Gravitational Potential

In highly symmetric systems (for example, spherical systems), the potential in TeVeS can be approximated by a MOND potential (just like GR can be approximated by Newtonian dynamics). The MOND gravitational potential ϕ is determined by the equation

$$\boldsymbol{\nabla} \cdot [\mu(|\boldsymbol{\nabla}\phi|/a_0)\boldsymbol{\nabla}\phi] = 4\pi G\rho \tag{2.17}$$

where ρ is the mass density and $a_0 \approx 10^{-8}\mathrm{cms}^{-2}$ is the MOND characteristic acceleration. The function μ is required to satisfy $\mu(x \gg 1) \approx 1$, so that Newtonian dynamics is recovered in the limit of large accelerations and $\mu(x \ll 1) \approx x$.

Note that the Newtonian gravitational potential ϕ_N is determined by the Poisson equation $\nabla^2\phi_N = 4\pi G\rho$ and that the Newtonian acceleration is given by $\boldsymbol{g}_N = -\boldsymbol{\nabla}\phi_N$. MOND acceleration is defined as $\boldsymbol{g} = -\boldsymbol{\nabla}\phi$. Newtonian acceleration g_N and MOND acceleration g are then related through a curl field (Bekenstein and Milgrom 1984):

$$\mu(g/a_0)\boldsymbol{g} = \boldsymbol{g}_N + \nabla \times \boldsymbol{h}. \tag{2.18}$$

In highly symmetric systems (i.e. those with spherical, planar, or cylindrical symmetry), the second curl term in Eq.(2.18) vanishes (Bekenstein and Milgrom 1984) and we have the exact result

$$\mu(g/a_0)\boldsymbol{g} = \boldsymbol{g}_N. \tag{2.19}$$

Thus, although equation (2.17) is non-linear and difficult to solve in general, in a highly symmetric system obtaining MOND acceleration $\boldsymbol{g}$ from the Newtonian acceleration $\boldsymbol{g}_N$ is straightforward.

In general cases, the curl term in Eq.(2.18) does not vanish, but it can be neglected at large distances from a bound object. Bekenstein and Milgrom (1984) have shown

that this curl term decreases faster with r than the other two terms:

$$\mu(g/a_0)\boldsymbol{g} = \boldsymbol{g}_N + O(r^{-3}) \tag{2.20}$$

If we choose $\mu(x \ll 1) = x$ for MOND region, then

$$g^2 = a_0 g_N + O(r^{-3}) => g = \sqrt{a_0 g_N + O(r^{-3})} \tag{2.21}$$

Since $\sqrt{a+b} < \sqrt{a} + \sqrt{b}$ $(a > 0, b > 0)$, then we have

$$g < \sqrt{a_0 g_N} + \sqrt{O(r^{-3})}, \tag{2.22}$$

i.e.

$$0 < g - \sqrt{a_0 g_N} < \sqrt{O(r^{-3})} \approx O(r^{-1.5}) \tag{2.23}$$

Based on the inequality (2.23), we use the approximation $\boldsymbol{g} \approx \sqrt{a_0 g_N}\boldsymbol{g}_N/g_N$ for a three-dimension elliptical mass distribution in Chapter 3.

2.3.2 Calculate weak lensing signals in MOND

We know in the spherical systems tangential shear γ_t is related to the convergence κ by Equation (2.14). In MOND, the real mass density ρ is replaced by the effective density ρ_{eff}, which is defined by (analogous to $\rho = \nabla^2\phi_N/4\pi G$.)

$$\rho_{eff} = \nabla^2\phi/4\pi G \tag{2.24}$$

Considering $\nabla^2\phi = \nabla \cdot (\nabla\phi) = \nabla \cdot (-g)$ and considering that g can be solved in Eq.(2.19) (given an explicit form of the μ function), we can obtain $\nabla^2\phi$ through the known Newtonian acceleration g_N. In the other words, we can get the effective density ρ_{eff} through g_N.

Once we know the effective density ρ_{eff}, we can get the corresponding effective

projected surface density Σ_{eff} by integrating it along the line of sight, i.e.

$$\Sigma_{eff}(x,y) = \int_{-\infty}^{+\infty} \rho_{eff}(x,y,z)\, dz. \tag{2.25}$$

The convergence κ_{mond} in MOND is given by

$$\kappa_{mond}(x,y) = \Sigma_{eff}(x,y)/\Sigma_{cr}, \Sigma_{cr} = \frac{c^2}{4\pi G}\frac{D_s}{D_L D_{LS}}. \tag{2.26}$$

Substituting the MOND convergence κ_{mond} into equation (2.14), we can get the tangential shear γ_t in MOND.

2.3.3 Comparing lensing signals in GR and MOND

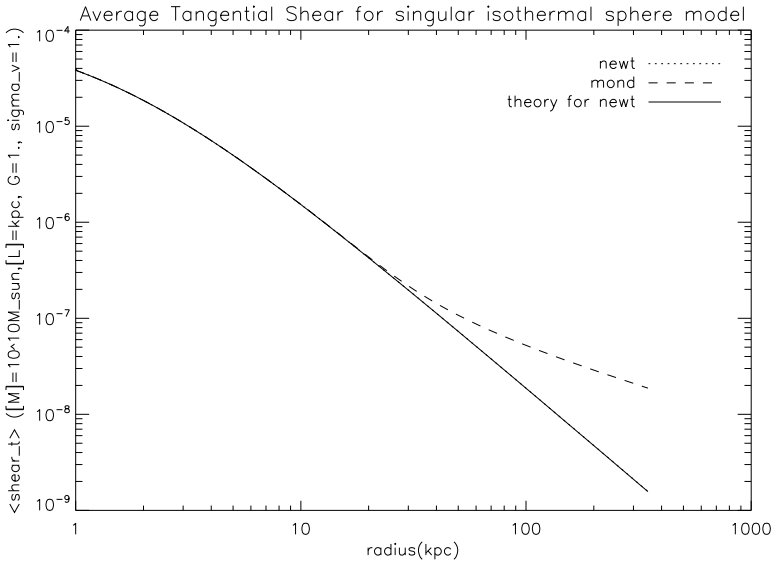

Figure 2.3: The difference between tangential shear γ_t in GR and MOND only happens at large radii for a given density model. In this plot, the density model is the singular isothermal sphere.

Since MOND modifies Newtonian gravity at low acceleration (i.e. large radii), the lensing signals from the Newtonian framework and the MOND framework should be expected to be different only at large radii. Fig. 2.3.3 shows the different tangential shears in GR and MOND for a SIS profile. They do indeed diverge only and most

significantly at large radii.

2.4 Density Profiles

In this part, we address the question of whether there is a difference in the weak lensing signals produced by galaxies of different density profiles.

We consider three different density profiles. For each profile, we require that 80% of the mass of the galaxy is within a radius of 10 kpc and they have the same total mass. These three density profiles are:

(1) Hernquist model. The density profile is (Binney and Tremaine 1987)

$$\rho(r) = \frac{M}{2\pi}\frac{a}{r}\frac{1}{(r+a)^3} \tag{2.27}$$

where M is the total mass and a is the scale length. We require a scale length $a = 1$ kpc.

(2) Exponential disk. The surface density is (Binney and Tremaine 1987)

$$\Sigma(r) = \Sigma_0 e^{-r/r_d} \tag{2.28}$$

where r_d is the disk scale length. Here we require a scale length $a = 3.5$ kpc.

(3) Kuzmin disk. The surface density is (Binney and Tremaine 1987)

$$\Sigma(r) = \frac{aM}{2\pi(r^2+a^2)^{3/2}} \tag{2.29}$$

where M is the total mass and a is the scale length. This requires a scale length $a = 2$ kpc.

For a galaxy of mass $M = 10^{12}M_\odot$, the calculation of convergence κ is shown in Fig. 2.4 The calculation of tangential shear γ_t is shown in Fig. 2.4. In each plot, the left panel is the result using Newtonian gravity, and the right panel is the result

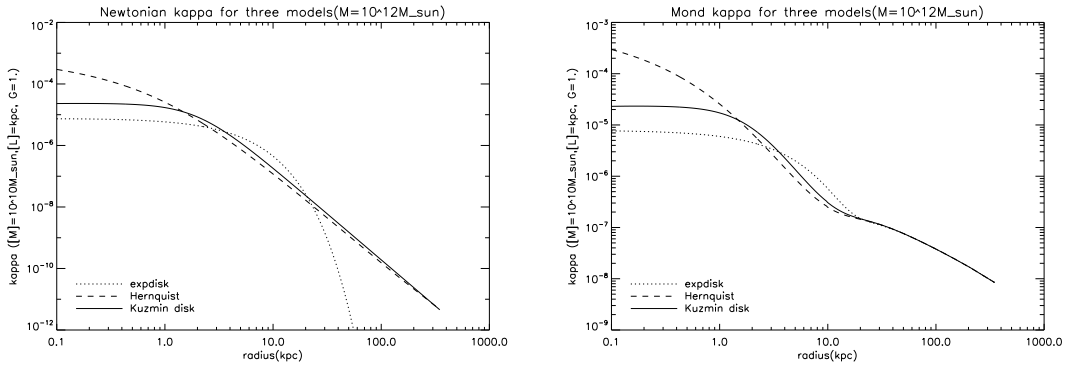

Figure 2.4: Left: Convergences κ for three density models using Newtonian gravity. Right: Convergence κ for three density models using MOND. These three density models are Hernquist model, exponential disk and Kuzmin disk (see the context for the specific definitions for these three models). The total mass of the galaxy is $M = 10^{12} M_{\odot}$. For each model, 80% of the mass of the galaxy is within a radius of 10 kpc.

using MOND. Fig. 2.4 shows different density profiles produce different tangential shears only at small scales. At large scales, the differences vanish: the $\gamma_t(r)s$ beyond the radius $r \approx 20$ kpc are almost identical for these three density models. Because these three density profiles have little similarity, we can infer that the difference between the density profiles would not produce a significant difference in the signals (tangential shear) at large radii.

What's more, the two plots in Fig. 2.4 show such a result does not hold only in the Newtonian framework but also in the MOND framework. This is a very useful result, because we can choose the most convenient density profile for a given specific problem. For example, in chapter 3, we choose a Singular Isothermal Sphere model for the calculation in GR and a point mass model for the calculation in MOND.

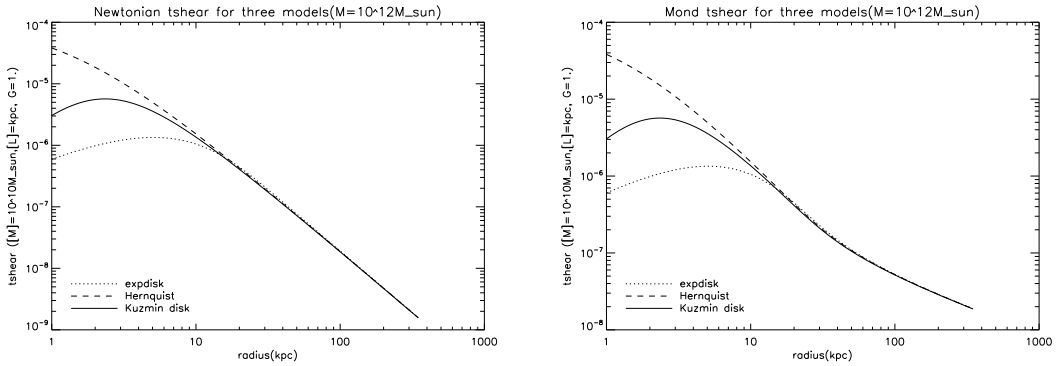

Figure 2.5: Left: Tangential shear γ_t for three density models using Newtonian gravity. Right: Tangential shear γ_t for three density models using MOND. These three density models are Hernquist model, exponential disk and Kuzmin disk (see the context for the specific definitions for these three models). The total mass of the galaxy is $M = 10^{12}\ M_\odot$. For each model, 80% of the mass of the galaxy is within a radius of 10 kpc. The plots in both panels show $\gamma_t(r)$ beyond the radius $r \approx 20$ kpc are virtually the same for these three density models. This means in both the Newtonian framework and the MOND framework, the different density profiles do not produce a significantly different lensing signal at large radii.

Chapter 3

Scaling Relation

3.1 Introduction

It is now well established that there are significant discrepancies between the Newtonian gravitational mass and the observable luminous mass on scales ranging from galaxies to clusters of galaxies[1]. Two fundamentally different explanations have been proposed to solve these observations: dark matter and MOND.

The dark matter scenario fits a range of galactic and cosmological observations. The current lack of a direct detection of the dark matter particle, however, has led to an alternative approach - MOND - to explain the observations. MOND works well on galactic scales. Recently, a cosmological model based on Tensor-Vector-Scalar gravity (TeVeS; MOND's relativistic form) and neutrino predicts the observed first two peaks of the power spectrum of Cosmic microwave background radiation (CMB). It seems MOND has become a competitive theory to challenge the dark matter scenario, therefore it becomes interesting to distinguish dark matter and MOND.

Most (dynamical) tests have focused on galactic scales (Read and Moore 2005; Famaey and Binney 2005; Zhao and Famaey 2006; Nipoti et al. 2007; Corbelli and Salucci 2007; Gentile et al. 2007). There are a few tests on sub-galactic scales using

[1]This chapter has been submitted as a paper to Monthly Notices of the Royal Astronomical Society.

the velocity dispersion of globular clusters (Baumgardt et al. 2005) and using the tidal radius (Zhao 2005; Zhao and Tian 2006).

Our approach to test MOND differs from previous studies in a number of ways. Unlike GR, MOND is a non-linear gravity theory, resulting in fundamental differences in their global scaling relations. Hence, rather than comparing the strength of the gravitational potential, we focus on how it changes with (baryonic) mass, although we do consider an example of the former as well. A fundamental property of MOND is its 'prediction' of a Tully-Fisher relation (Tully & Fisher 1977). In MOND this relation follows from the theory (Milgrom 1983a), whereas in ΛCDM it arises from the interplay between dark and baryonic matter. Also note that observationally the Tully-Fisher relation is one between the luminosity and the (maximum) rotation velocity, and thus is a test of theory on sub-galactic scales.

It is therefore useful to examine MOND on scales much larger than those probed by rotation curves. Probing the gravitational potential in these outer regions of galaxies provides an ideal test of alternative gravity, because of the absence of luminous matter (except for a few satellites and globular clusters). It is in these regions where MOND and ΛCDM differ most markedly. In the dark matter paradigm we would call these regions 'dark matter dominated' and in MOND we call them 'deep-MOND regions'. Finally, rather than dynamics, we will study the gravitational lensing signal around galaxies.

We note that other tests involving (strong) gravitational lensing already have provided important constraints, albeit on relatively small scales. These studies typically reveal a factor of two discrepancy between stellar mass and the lensing mass using MOND (Zhao et al. 2006; Chen and Zhao 2006; Angus et al. 2007; Ferreras et al. 2008).

To probe the outer regions around galaxies we employ a technique called weak gravitational galaxy-galaxy lensing (hereafter g-g lensing), which is the statistical

study of the deformation images of distant galaxies by foreground galaxies. Since the gravitational distortions induced by an individual lens are too small to be detected, one has to resort to the study of the ensemble averaged signal around a large number of lenses. Of particular interest is that the g-g lensing signal can be measured out to large projected distance, where dynamical methods are of limited use due to the lack of luminous tracers. Hence, g-g lensing provides a unique and powerful tool to probe the gravitational potential on large scales. Only studies of satellite galaxies can also probe these regions (Zaritsky and White 1994; McKay et al. 2002; Prada et al. 2003; Conroy et al. 2007).

Since the first detection by Brainerd et al. (1996), the accuracy of g-g lensing studies has improved dramatically thanks to improved analysis techniques and large amounts of wide-field imaging data (Fischer et al. 2000; Hoekstra et al. 2004, 2005; Mandelbaum et al. 2006b; Parker et al. 2007). We refer to these papers for a more in-depth discussion of this area of research. Relevant for our study is the availability of (photometric or spectroscopic) redshift information for the lens galaxies. Only recently has this kind of information become available for large samples (Hoekstra et al. 2005; Mandelbaum et al. 2006b). As a result we can now compare how the strength of the g-g lensing signal depends on the baryonic content of the lenses.

This chapter is organized as follows. In §3.2, we discuss the expected dependence of the lensing signal on stellar mass. In §3.3 we describe the galaxy-galaxy lensing data used in our analysis. In §3.4 we present our results and discuss the implications for MOND.

3.2 Theoretical Predictions

One of the reasons for the success of MOND is the ability to provide excellent fits to rotation curves over a wide range in mass, thanks to its 'built-in' Tully-Fisher relation (Milgrom 1983a). As we show below, this feature has consequences for the

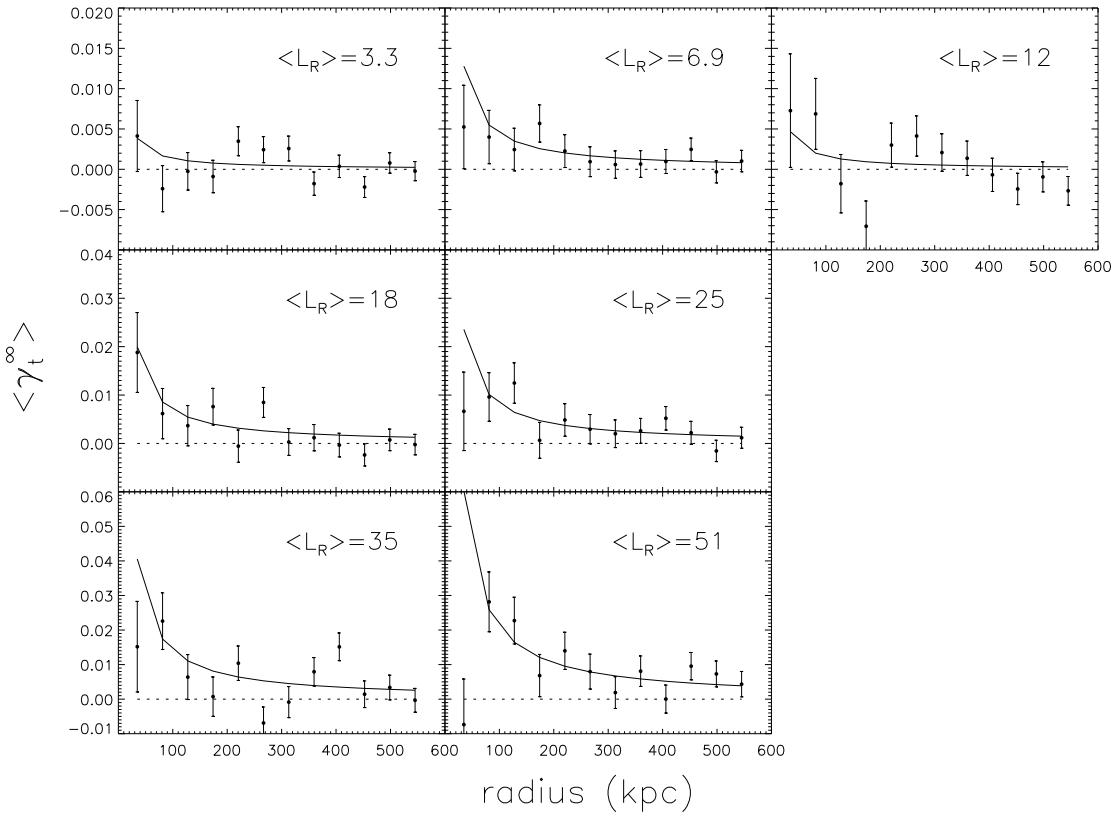

Figure 3.1: The observed ensemble averaged tangential shear around 'isolated' galaxies from Hoekstra et al. (2005). The data are shown for 7 luminosity bins (with the mean L_R indicated in units of $10^9 L_{R,\odot}$). The solid line indicates the best fit SIS model. The lensing signal has been scaled to that of a lens at the average lens redshift ($z \sim 0.32$) and a source redshift of infinity.

predicted scaling of the lensing signal with stellar mass.

In the context of GR, the galaxy-galaxy lensing signal within ~ 400 kpc is well described by a Singular Isothermal Sphere (SIS) model (Hoekstra et al. 2004) with

$$\rho(r) = \frac{\sigma_v^2}{2\pi G r^2},$$

where σ_v is the line-of-sight velocity dispersion. The corresponding azimuthally averaged tangential shear (which corresponds to the observed g-g lensing signal) is given by

$$\langle \gamma_t \rangle (r) = \frac{r_E}{2r}, \tag{3.1}$$

where r_E is the Einstein radius, which is related to σ_v through

$$r_E = 4\pi \left(\frac{\sigma_v}{c}\right)^2 \frac{D_{ls}}{D_s}, \tag{3.2}$$

and where D_{ls} and D_s are the angular diameter distances between the lens and the source, and the observer and the source, respectively. Hence the observed value of the Einstein radius provides a convenient measure of the amplitude of the lensing signal. Simulations of dark matter halos in ΛCDM predict a somewhat different density profile (e.g., Navarro, Frenk & White 1995) but our results do not depend on the adopted profile.

In MOND the only source of gravity is the luminous matter. As we are concerned with the lensing signal on large scales, we assume that the galaxy (stellar) mass distribution can be approximated by a point mass model. We have verified that the lensing signal on large scales (> 20 kpc) is insensitive to the actual baryonic density profile. Under these assumptions the MOND effective density $\rho_{\rm eff}$ for a point mass with mass M is given by

$$\rho_{\rm eff}(r) = \frac{\nabla^2 \Phi}{4\pi G} = \frac{v_0^2}{4\pi G} \frac{1}{r^2}, \tag{3.3}$$

where Φ is the gravitational potential in MOND, $v_0 \equiv (GMa_0)^{\frac{1}{4}}$ and a_0 is the MOND critical acceleration ($a_0 \approx 10^{-8}\mathrm{cms}^{-2}$). We assumed that $r \gg r_0 \equiv \sqrt{GM/a_0}$. For a mass $M = 10^{11}M_\odot$, we find $r_0 \approx 10\mathrm{kpc}$, which is much smaller than the scales we probe in this paper. Once we have obtained the effective density ρ_{eff}, we can apply the same procedure as in the GR case to calculate the tangential shear (Zhao 2006). The effective surface density is given by

$$\Sigma(r) = \frac{v_0^2}{4G}\frac{1}{r}. \tag{3.4}$$

The convergence κ is the ratio of the surface density and the critical surface density Σ_{crit}, which is given by

$$\Sigma_{\mathrm{crit}} = \frac{c^2}{4\pi G}\frac{D_s}{D_l D_{ls}}, \tag{3.5}$$

where D_{ls} is the distance from the lens to the source and D_l and D_s are the distances from the observer to the lens and the source, respectively. We use the fact that the tangential shear γ_t is related to the convergence through $\gamma_t = \bar{\kappa}(< r) - \kappa(r)$, where $\bar{\kappa}(< r)$ is the mean convergence within the radius r. This yields a convergence κ and tangential shear γ_t given by

$$\kappa(r) = \gamma_t = \frac{\Sigma(r)}{\Sigma_{\mathrm{crit}}} = \frac{v_0^2}{4G\Sigma_{\mathrm{crit}}}\frac{1}{r}. \tag{3.6}$$

Hence MOND predicts a tangential shear profile that mimics that of an SIS model, but with an Einstein radius

$$r_E = 2\pi\left(\frac{v_0}{c}\right)^2\frac{D_{ls}}{D_s}. \tag{3.7}$$

Although similar in appearance, the physical interpretations are markedly different. This becomes apparent when we consider the dependence of the Einstein radius on mass. In the GR case we have

$$r_E \propto \sigma_v^2 \propto M. \tag{3.8}$$

We expect a linear relation between the total galaxy mass (within a fixed radius) and Einstein radius r_E. In the MOND case, however, we have $v_0^2 \propto \sqrt{M}$ (as $v_0 \equiv (GMa_0)^{\frac{1}{4}}$), which yields

$$r_E \propto v_0^2 \propto \sqrt{M_*}, \tag{3.9}$$

where we explicitely use the stellar mass M_* as the mass of a galaxy (we ignore the contribution from gas). Therefore MOND predicts a Tully-Fisher-like scaling relation between the Einstein radius and the stellar mass. In the GR case, the total mass depends on the relative contributions of dark and luminous matter, thus preventing us from predicting the value of the slope.

3.3 Observational Data

The measurement of the g-g lensing signal as a function of stellar mass requires a large data set of sources and lenses with redshift information. As a further complication, the predictions given in §2 are only valid for an isolated galaxy. If the lensing signal includes a significant contribution from nearby galaxies, galaxy groups or clusters, then the inferred Einstein radius will be biased. This is particularly relevant for faint galaxies (see Fig 7. in Hoekstra et al. (2005)). To ensure that the observed lensing signal is that of the lens galaxy itself, we consider two particular data sets which are described in more detail below.

3.3.1 Red-sequence Cluster Survey (RCS)

The Red-sequence Cluster survey (RCS) is a galaxy cluster survey using R_c and z' imaging data (Gladders and Yee 2005). Within the surveyed area, ~ 33.6 deg^2 were also imaged in the B and V bands. The four-filter data in the latter area were used

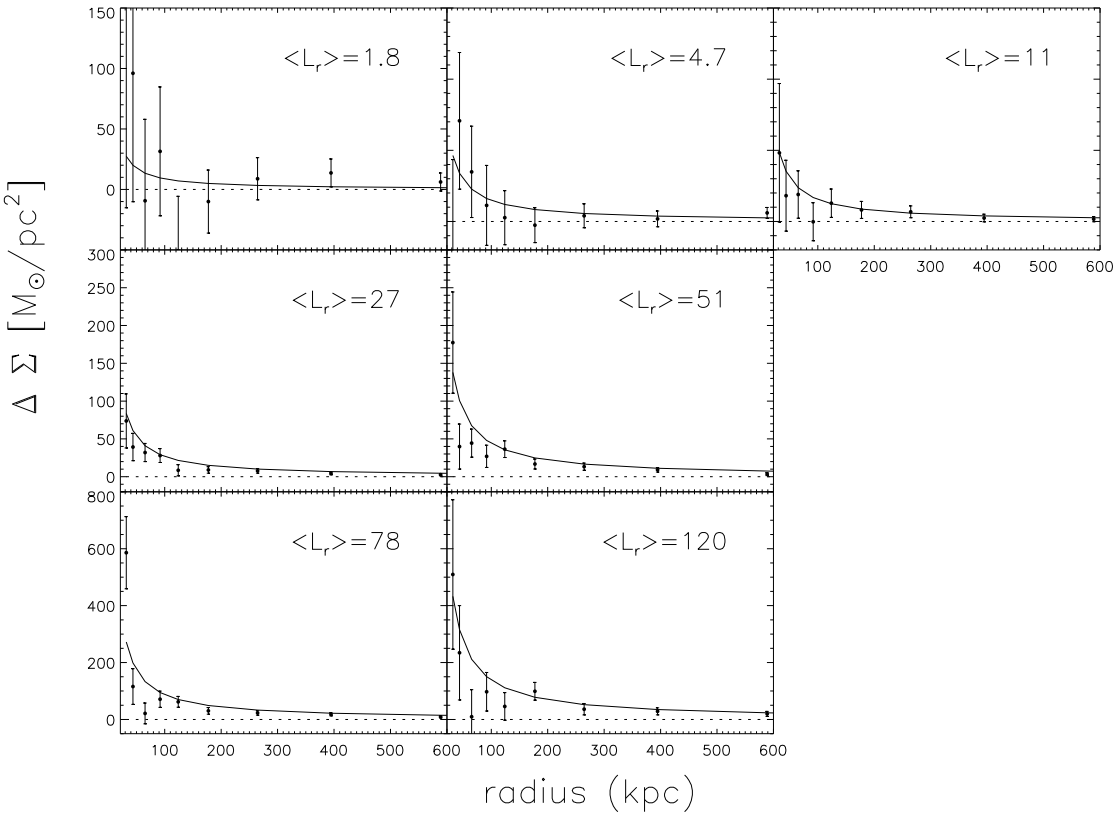

Figure 3.2: The observed galaxy-galaxy lensing signal around early type galaxies in low density regions from (Mandelbaum et al. 2006b). The data are shown for 7 luminosity bins (with the mean L_r indicated in units of $10^9 L_{r,\odot}$). The solid line indicates the best fit SIS model. In order to extract the signal dominated by the lens galaxy itself, we fit the signals only within ~ 200 kpc from the lens.

by Hsieh et al. (2005) to derive photometric redshifts for 1.2×10^6 galaxies, which were used by Hoekstra et al. (2005) to study the weak lensing signal as a function of galaxy properties. H05 selected a sample of 'isolated' lens galaxies by ensuring that no galaxy more luminous than the lens was located within 30". Hence the galaxies in the faintest bin are truly isolated, whereas the brightest galaxies can have nearby (faint) companions.

The 'isolated' lens sample comprises of 94,509 galaxies with $0.2 < z < 0.4$ and restframe R_C luminosities. For the analysis we limit the measurement of the lensing signal to within 600 kpc from the lens. Figure 3.1 shows the observed tangential shear profiles and the best fit SIS model. As discussed in Benjamin et al. (2007) the mean source redshift used in H05 was biased low because of the lack of a reliable training set at high redshift. Consequently the masses listed in H05 were biased high by $\sim 15\%$ compared to the results used here. The luminosity shown in the plots is the mean rest-frame R band luminosity in units of $10^9 L_{R,\odot}$. Finally, random errors in the photometric redshift estimates of the lenses lead to an underestimate of the true value of r_E, which we correct for as in H05.

3.3.2 Sloan Digital Sky Survey (SDSS)

Mandelbaum et al. (2006; M06) studied the g-g lensing signal using data from the SDSS survey (York et al. 2000), with the lenses selected from the SDSS Data Release Four main spectroscopic sample (DR4; Adelman-McCarthy 2006) which covers 4783 deg^2. The lens galaxies have spectroscopic redshifts between $0.02 < z < 0.35$. M06 split their sample into early and late type galaxies, based on morphology. The early-type galaxies are also divided into overdense and underdense samples based on the median local galaxy environment density within each luminosity bin. We use the results for the latter sample (Fig. 3, black triangles in M06), because we expect the contribution of neighboring galaxies to the g-g lensing signal to be reduced. Limiting the sample to early type galaxies also reduces the variation of stellar mass-to-light

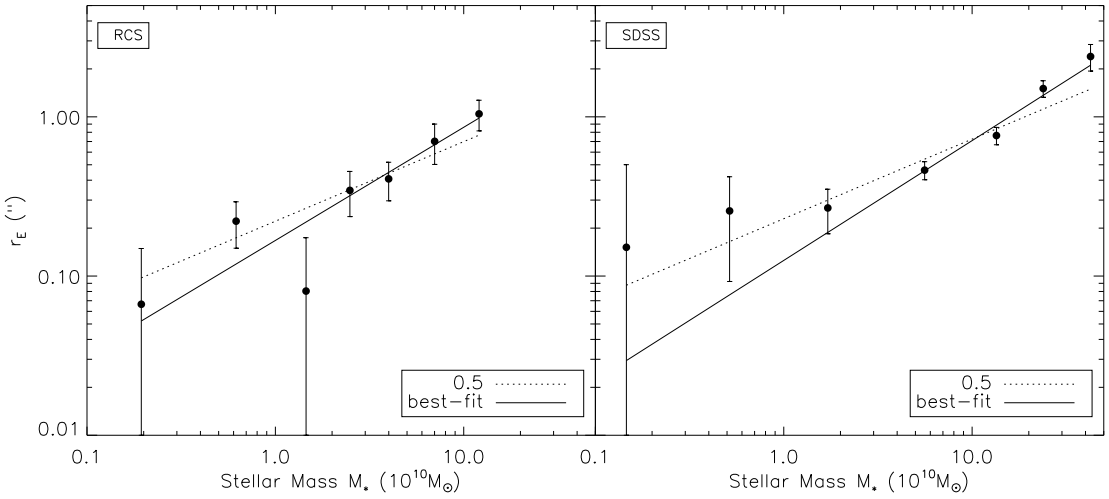

Figure 3.3: *Left panel:* Einstein radius r_E as a function of stellar mass for the RCS data from Hoekstra et al. (2005). *Right panel:* Value for r_E obtained from the SDSS g-g lensing signal from Mandelbaum et al. (2006b). To allow for a simple comparison, all Einstein radii in the plot have been scaled such that $D_{ls}/D_s = 1$. The dotted line in each plot represents the best fit assuming $r_E \propto \sqrt{M_*}$ (as predicted by MOND). The best fit power law is indicated by the solid line.

ratio with luminosity.

M06 represent the lensing signal by $\Delta\Sigma(r)$, where $\Sigma(r)$ is the projected surface density:

$$\Delta\Sigma(r) \equiv \bar{\Sigma}(< r) - \Sigma(r) = \langle\gamma_t\rangle\Sigma_{\rm crit}. \tag{3.10}$$

The resulting tangential shear profiles are presented in Figure 3.2. Although the lenses are selected to be in underdense environments, it is possible that lens galaxies in low luminosity bins (e.g. L1, L2 and L3) are surrounded by luminous galaxies. Hence the lensing signals in these low luminosity bins could include a non-negligible contribution from the surrounding brighter galaxies. Theoretical analysis of the expected g-g lensing signal suggests the group and cluster haloes can dominate the lensing signal on scales larger than 300 kpc (Seljak 2000). The signal on scales less than ~ 200 kpc is expected to be dominated by the lens itself. Therefore we fit a SIS model only to the measurements within 200 kpc. The best fit models are represented by the solid lines in Figure 3.2. Note that despite our concerns, the best fit model is

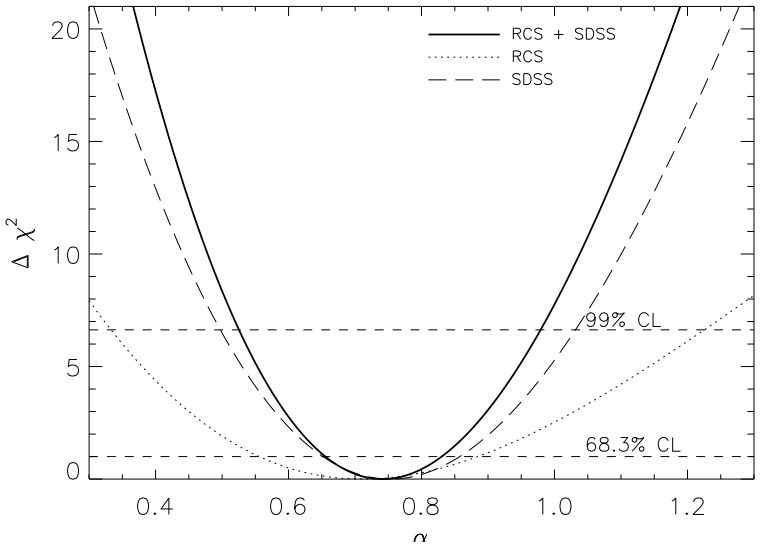

Figure 3.4: $\Delta\chi^2$ as a function of the exponent α in the power-law relation $r_E \propto M_*^{\alpha}$, while marginalizing over the normalization. The dotted line corresonds to the constraints from a fit to the RCS results, whereas the long-dashed line is the result from the SDSS data. The solid line is the combined constraint. These results indicate that $\alpha > 0.5$ (with 99.7% confidence) and thus inconsistent with the MOND prediction

an excellent fit to the points at large radii and extending the fits to larger radii does not change our results.

3.3.3 Stellar masses

M06 also present estimates for the stellar masses. The procedure used by M06 is based on the same techniques as in Kauffmann et al. (2003) and the stellar masses are derived from a comparison of a library of star formation history models to the spectroscopic data. We use the observed (power law) relation between stellar mass and luminosity to convert the luminosities listed in Figure 3.2. The derived stellar mass depends predominantly on the adopted low-mass end of the initial mass function. This leads to an uncertain normalisation, but the inferred dependence of stellar mass with luminosity is robust (Bell and de Jong 2001).

Unlike the SDSS data, the RCS results lack a detailed estimate of stellar masses. However, in addition to numbers for early type galaxies, M06 also provide stellar

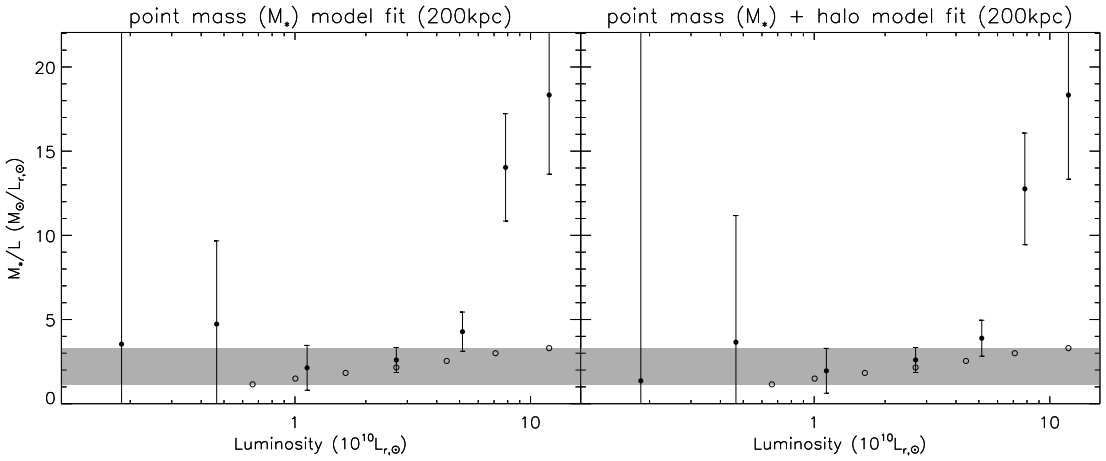

Figure 3.5: *Left panel:* the derived MOND mass-to-light ratio as a function of luminosity. The derived MOND masses are obtained by fitting a point mass model to the SDSS data within 200 kpc. Because there is no dark matter in MOND, we take the derived MOND mass to be the total stellar mass M_* (we can ignore the contribution from HI). *Right panel:* The MOND mass-to-light ratio from a fit to the SDSS data when we add a neutrino halo to the stellar mass. The neutrino halo is assumed to have a β profile and its total mass is three times of the stellar mass. The stellar mass-to-light ratios as a function of luminosity from Mandelbaum et al (2006) are indicated by the open circles. The shaded area indicates the range in those inferred stellar mass-to-light ratios.

masses for late type galaxies and list the fraction of late types as a function of luminosity. We use these results to compute the stellar mass as a function of luminosity for the RCS2 data. H05 computed stellar mass-to-light ratios as a function of color using the results from Bell and de Jong (2001). We compared these (less accurate) results to our estimates based on the numbers provided in M06 and find good agreement.

3.4 Results

Figure 3.3 shows the measurement of the Einstein radius as a function of the stellar mass of the lens. The left panel shows the results for the RCS data and the right panel corresponds to the results for the SDSS data. The Einstein radii in Fig. 3.3 have been scaled to $D_{ls}/D_s = 1$. We assume a power-law relation between the Einstein radius and the stellar mass: $r_E \propto M_*^{\alpha}$. For reference, the dotted lines in Figure 3.3 show the best fit relation for $\alpha = 0.5$, which is the expected slope for MOND.

Before we proceed with our determination of the scaling relation between lensing signal and stellar mass, we first examine whether the amplitudes of the signal agree between RCS and SDSS. For the comparison we adopt $\alpha = 0.75$ and obtain a value of $r_E = 0\farcs52 \pm 0\farcs06$ for a galaxy with a stellar mass of $M_* = 5 \times 10^{10} M_\odot$ for the RCS measurements. For the SDSS data we obtain a value of $r_E = 0\farcs42 \pm 0\farcs03$, in fair agreement with the RCS results.

For the RCS data we find a best fit power-law slope of $\alpha = 0.71 \pm 0.15$ ($\chi^2_{\rm min} = 4.5$ for 5 degrees of freedom; we marginalize over the normalization). The difference in χ^2 ($\Delta\chi^2 = \chi^2 - \chi^2_{\rm min}$) as a function of α is indicated by the dotted line in Figure 3.4. For the SDSS data we find $\alpha = 0.75 \pm 0.09$ ($\chi^2_{\rm min} = 4.9$ for 5 degrees of freedom) and the corresponding $\Delta\chi^2$ is indicated by the long-dashed curve in Figure 3.4. Combining the RCS and SDSS constraints yields a value $\alpha = 0.74 \pm 0.08$. (solid line in Figure 3.4). Hence we find good agreement between the RCS and SDSS data, with the SDSS data providing the best contraint. This result is also in good agreement with Conroy et al. (2007) who found that the velocity dispersion of satellite galaxies scales with the stellar mass of the host galaxy $\sigma \propto M_*^{0.4 \pm 0.1}$, which corresponds to $r_E \propto M_*^{0.8}$ for an isothermal sphere model.

The inferred slope for the combined data is larger than $\alpha = 0.5$ (which is the value predicted by MOND) with 99.7% confidence. The slope does depend on the stellar masses, but as argued in §3.3 we expect this to be a small effect.

An alternative way to present our measurements is to consider the mass-to-light ratio as a function of luminosity. We expect the inferred MOND mass-to-light ratio to correspond to the stellar mass-to-light ratio, because in this case the stellar mass is the only source of gravity (we can ignore the contribution from neutral hydrogen). The left panel in Figure 3.5 shows the derived MOND mass-to-light ratio as a function of luminosity. The mass is determined from a fit to the SDSS lensing signal out to 200 kpc, assuming a point mass model for the galaxy.

Interestingly, at low luminosities the mass-to-light ratio is constant with values in agreement with what one might expect for an old population (the shaded region indicates the range of stellar M/L from Mandelbaum et al., 2006). At high luminosities, however, we observe a significant increase in M/L which are inconsistent with the expected values for the stellar populations. Hence, these measurements suggest the need for additional (dark) matter.

3.4.1 Potential biases

The data points at high stellar mass in Figure 3.3 (and at high luminosity in Fig. 3.5 as well) carry much of the statistical weight, both for RCS and SDSS. It is apparent that if we were to remove or lower those measurements, the remaining data suggest a slope consistent with the MOND prediction, instead of the steeper relation determined in the previous section. Here we argue that those data points cannot be ignored, because they are in fact the more reliable measurements.

Compared to brighter galaxies, the lensing signal around a faint galaxy is more easily affected by the contribution of neighboring bright galaxies. Although we have selected 'isolated' or underdense lens samples for our analysis, the lensing signal in the low luminosity bins is potentially biased to higher values, thus lowering the inferred slope. In contrast, this will not be significant for the high luminosity bins, especially on small scales. To investigate this further we examined the effect of environment on the lensing signal around bright galaxies. The panels for L5b and L6f in Figure 3 from Mandelbaum et al. (2006b) correspond to our two highest luminosity bins. These results suggest there are no significant differences in the lensing signals on small scales ($\sim$ 200 kpc) between the overdense and underdense samples. This implies that on these small scales the contribution of the environment to the lensing signals is negligible and the signal is dominated by the lens itself. Finally, the agreement between the RCS and SDSS results, which are based on different selection algorithms for the lenses, suggest the measurements are robust.

3.4.2 Neutrino Halos

The arguments presented in the previous section suggest the need for dark matter in luminous galaxies, even in the context of MOND. Similarly, MOND cannot explain observations of clusters of galaxies without invoking a significant dark matter component (Sanders 2007): the MOND dynamical mass is about a factor $3-4$ times larger than the observed baryonic mass. Sanders (2007) suggests that neutrinos with a mass $m_\nu \sim 2eV$ might be responsible for this mass discrepancy. In this section we examine the effect of such a massive neutrino halo on the observed g-g lensing signal.

We do so by adding a neutrino halo model to the stellar component (which is approximated by a point mass). Following Sanders (2007), we assume that the neutrino halo follows a β-model profile (with $\beta = 1$) and that the total halo mass is three times that of the stellar mass. The factor three is a cosmological constraint, which also matches the required amount to explain the MOND masses of galaxy clusters (Sanders, 2007). We have also verified that our results do not depend on the adopted value of β (a value of 0.6 gives very similar results). The neutrino halo profile is given by:

$$\rho(r) = \rho_0 \left[1 + \left(\frac{r}{R_c}\right)^2\right]^{-1.5}, \tag{3.11}$$

where ρ_0 is the central density

$$\rho_0 = \frac{M_\nu}{\frac{4}{3}\pi {R_c}^3} = \frac{3M_*}{\frac{4}{3}\pi {R_c}^3}, \tag{3.12}$$

and the core radius R_c is given by Sanders (2007)

$$R_c = 1.8 \left(\frac{m_\nu}{1eV}\right)^{-4/3} \left(\frac{M_\nu}{10^{14} M_\odot} \frac{1}{0.06}\right)^{\frac{1}{12}} \text{ Mpc}. \tag{3.13}$$

As mentioned above, we take $M_\nu = 3M_*$. Hence the stellar mass is the only

parameter in the fit. Figure 3.6 shows the best fit model to the SDSS measurements for the highest luminosity bin. The model is fitted to the measurements within 200 kpc. We find a core radius $R_c = 720$ kpc. Figure 3.6 shows that on these scales the stellar component dominates the lensing signal and that the neutrino halo only becomes relevant on large scales. This may seem surprising because the neutrino halo is much more massive than the stellar component. It is, however, important to remember that the weak lensing shear is really measuring mass contrasts: for instance, a constant sheet of matter does not introduce a shear (Gorenstein et al. 1988). As a result it is not the mass of the halo that is most relevant for our study, but the fact that the halo is very extended.

Consequently, the inferred stellar mass-to-light ratio is reduced only slightly compared to our original results. This is clearly demonstrated in the right panel of Figure 3.5, which shows the resulting mass-to-light ratios. We therefore conclude that including a neutrino halo around the lens galaxies cannot explain the high mass-to-light ratios.

A related issue arises from the fact that the most luminous galaxies are located in filaments. The filaments can in principle contribute a significant amount of mass along the line-of-sight, which was studied in Feix et al. (2007). In their model, the filament induces a shear which is uniform over scales much larger than the ones we study here. A constant shear will cancel when we compute the azimuthally averaged shear around the lenses, and we therefore argue that filaments do not affect our small scale g-g lensing signal.

Similar to massive clusters of galaxies, many elliptical galaxies are surrounded by hot, ionized gas. This gas is observed in X-ray observations (Humphrey et al. 2006) and we need to consider its impact on our results. Humphrey et al. (2006) used Chandra observations to study the ionized gas around NCG720, NGC4125 and NGC6482, which are three field ellipticals. Hence, these galaxies resemble the lenses

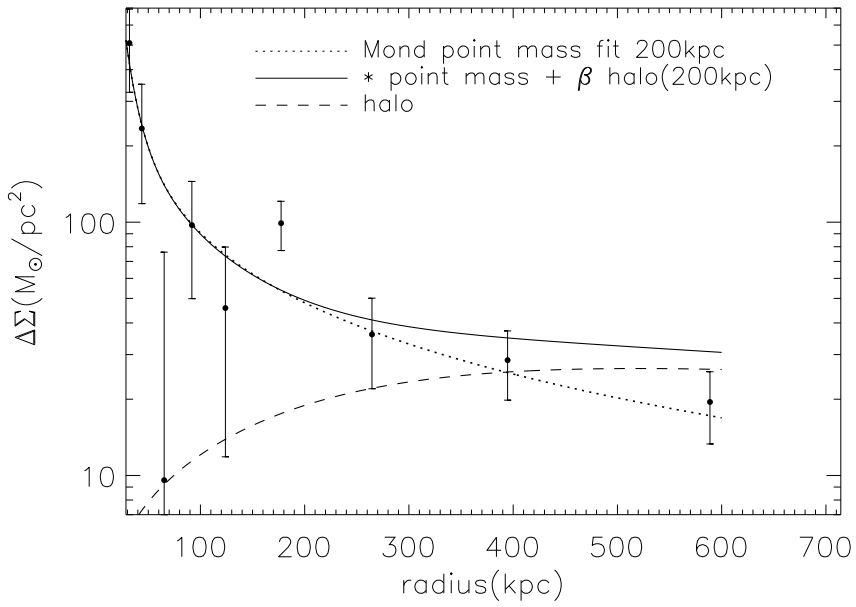

Figure 3.6: Fit to the SDSS data for the highest luminosity bin. A model consisting of a point mass of M_* (stellar component) and a neutrino halo with a mass $3 \times M_*$ is fitted to the measurements within 200 kpc. The compact stellar mass dominates the lensing signal on small scales and as a result, our results are insensitive to the effects of a neutrino halo.

studied in our analysis. In all three cases, the X-ray observations allow Humphrey et al. (2006) to study the relative distribution of the stars, gas and dark matter. From their Figure 6 it is clear that the gas is much more extended than the stellar mass. Furthermore, the amount of gas inferred from the data is less than the stellar mass within 200 kpc.

Because of its extent and relatively low mass, the contribution from the hot gas to the tangential shear is expected to be even smaller than that from a neutrino halo. To investigate this further, we considered a gas halo with a core radius of 30 kpc and a mass equal to the stellar mass. Although the smaller core radius boosts the shear on small scales compared to the neutrino halo, the resulting signal is a poor fit to the data, because it cannot reproduce the high lensing signal on small scales (while at the same time not overestimating the shear on large scales).

3.5 Conclusions

We study the amplitude of the weak gravitational lensing signal as a function of lens luminosity around a sample of relatively isolated galaxies. We demonstrate how such a study can be used to test Modified Newtonian Dynamics (Milgrom 1983b). Compared to previous work, our study is a test of MOND on relatively large scales, where the differences between MOND and ΛCDM are expected to be large. We show that MOND predicts a Tully-Fisher-like relation between the lensing signal (as quantified by the Einstein radius of a SIS model) and the stellar mass M_*.

Our analysis of data from RCS and SDSS shows that the amplitude of the lensing signal as a function of stellar mass is well described by a power law with a best fit slope of $\alpha = 0.74 \pm 0.08$. This result is inconsistent with $\alpha = 0.5$, the predicted slope of MOND. Uncertainties in the stellar popoulations used to derive the stellar masses are not expected to be small and should not alter our result.

As a related test, we determined the MOND mass-to-light ratio as a function of lens luminosity. Our results require dark matter to explain the amplitude of the lensing signal for the most luminous galaxies. We examined whether our findings can be reconciled with MOND by considering a massive neutrino halo. Such a halo is found to be too extended to produce a significant change in the g-g lensing signal on scales less than 200 kpc. Similarly, hot ionized gas observed around elliptical galaxies (Humphrey et al. 2006) cannot explain our results in the context of MOND.

Although in this paper we focussed on MOND, we note that our findings are relevant for any alternative theory of gravity. Such theories should not just attempt to explain the Tully-Fisher relation (i.e., the scaling of rotation curves on small scales), but also need to explain our lensing measurements. In our opinion this is an important (and non-trivial) test to pass. Finally we note that much larger surveys, such as the Canada-France-Hawaii Telescope Legacy Survey (CFHTLS),

will significantly improve in the coming years.

Chapter 4

Halo Shape

4.1 Introduction

The shape of the dark matter (DM) halo around a galaxy is intimately related to the process of galaxy formation. The properties of dark matter have implications for the halo shape. Different assumptions about dark matter predict different shapes of DM halos. N-body simulations of dissipationless dark matter with either no baryons or adiabatic hydrodynamics produce triaxial dark halos of $< c/a >= 0.5$ (Frenk et al. 1988; Dubinski and Carlberg 1991) where c/a is the ratio of the shortest to longest axes of the mass density of the halo. Due to their collisional behavior, the presence of baryons affects the shapes of halos. Simulations show adding a small fraction ($\sim 10\%$) of dissipative gas results in a moderately flattened shape (Katz and Gunn 1991; Dubinski 1994; Dubinski and Kuijken 1995). In addition, high resolution ΛCDM simulations show low-mass halos are rounder than high-mass halos and for a fixed mass, halos are rounder at low redshift (Thomas et al. 1998; Warren et al. 1992; Bullock et al. 2001; Allgood et al. 2006). Such results hint that the formation history of the galaxy plays a role in setting the halo shape. Therefore, the determination of the halo shapes of galaxies is important for it can be used to test our understanding of galaxy formation and dark matter.

The observation of the halo shape also plays a role in distinguishing alternative

theories of gravity from the dark matter paradigm, in particular Modified Newtonian Dynamics (MOND) (Milgrom 1983b). In MOND, baryonic mass can produce an effective halo, which is similar to the dark matter halo in the ΛCMD model. This effective halo in MOND is, however, fundamentally different from the dark matter halo. Generally, it has the following geometrical properties (Milgrom 2001; Sellwood and Kosowsky 2002): (i) an asymptotically spherical shape away from the center of galaxy; (ii) a highly flattened shape in the inner region; (iii) halo axes that are aligned with the light axes. We note that the properties of (i) and (ii) are opposite to DM halos in ΛCDM simulations (Springel et al. 2004).Therefore, a precise measurement of the halo shape can provide a critical test of MOND. Also, according to (iii), if we detect any offset between the halo axes and the light axes, then MOND and other alternative theories of gravity will be positively ruled out.

To observe the halo shape, there are three basic approaches. One is using dynamical measurements. By measuring anisotropic motions of stars, the ellipticity of the galaxy halo can be derived (Binney and Tremaine 1987; van der Marel 1991; Amendt and Cuddeford 1994). Due to using stars as the tracer, the results from this method have to be limited to the inner regions of a galaxy ($\sim$ 20 kpc). The second approach is observing isophotes of X-ray gas around isolated galaxies. Assuming hot gas in hydrostatic equilibrium, the shape of the gravitational potential can be derived, and therefore the shape of the DM halo (Buote and Canizares 1996, 1997, 1998). However, the question of whether or not assuming hydrostatic equilibrium is valid raises doubts about the robustness of the result. The third approach is gravitational lensing, which does not require assumptions about the dynamical state. Using the weak lensing technique, the lens galaxy can be explored out to large projected radii (hundreds of kpc). By measuring the azimuthal variation of the lensing signal, weak lensing provides constraints of the shapes of halos.

To test MOND using the azimuthal weak lensing signal was first proposed by

Mortlock and Turner (2001a,b). The exploration of this idea was hindered due to the low accuracy of g-g lensing measurement at that time. Our ability to make this measurement has improved dramatically since then. The difference in the lensing signal along different orientations can be detected (Hoekstra et al. 2004; Parker et al. 2007; Mandelbaum et al. 2006a).The first anisotropic lensing signal was reported by Hoekstra et al. (2004) using the R_c-band imaging data from the Red-sequence Cluster Survey (Gladders and Yee 2005).

As the second test, we compare the theoretical prediction of anisotropic lensing signals in MOND with the observation in Parker et al. (2007). This chapter is organized as follows. In §4.2 we describe our calculation of the lensing signal expected from MOND. In §4.3 we describe observational data used for comparison of MOND. In §4.4, we present the comparison results. In §4.5, we discuss effects from the environment on the results. We draw our conclusions in §4.6.

4.2 Anisotropic Shear in MOND

In the framework of MOND, visible mass is responsible for all of the observed properties. The mass distribution should explain anisotropic motions of halo stars, non-spherical distribution of hot gas around the host galaxy, and the observed anisotropic weak lensing signals.

In the following, we examine the anisotropic shear induced by the non-spherical visible mass distribution in MOND. For simplicity, we start with the mass distribution of an extremely high ellipticity. In our model, we assume the galaxy's geometry is such that $a = c = 30$ kpc, $b = 3$ kpc, where a, b and c are the semimajor axes, and c is along the line of sight. This three-dimensional distribution gives a projected ellipticity $b/a = 0.1$. In order to simplify the calculation, we assume the galaxy has a uniform density. We learned in Chapter 2 that the specific density profile does not affect the shear result on large scales. Given that we are comparing the anisotropic

shear over large scales (up to $250h^{-1}$ kpc), this simple assumption would not affect the final result.

In the following, we describe how to calculate shear for such a homogenous ellipsoid in MOND. The procedure is as follows.

(1) First, we already have the Newtonian gravitational potential $\Phi_N(x, y, z)$ for this mass distribution. Chandrasekhar (1969) gives $\Phi_N(x, y, z)$ as theorem 9 on p 49 in his book:

The Newtonian potential of a homogeneous ellipsoid E at an external point (x, y, z) *is given by*

$$\Phi_N(x, y, z) = \pi G\rho abc \int_\lambda^{+\infty} \frac{du}{\Delta}\left(1 - \left(\frac{x^2}{a^2+u} + \frac{y^2}{b^2+u} + \frac{z^2}{c^2+u}\right)\right) \tag{4.1}$$

where

$$\Delta^2 = (a^2+u)(b^2+u)(c^2+u) \tag{4.2}$$

and λ *is the ellipsoidal coordinate of the point considered: that is the positive root of the equation*

$$\frac{x^2}{a^2+\lambda} + \frac{y^2}{b^2+\lambda} + \frac{z^2}{c^2+\lambda} = 1 \tag{4.3}$$

(2) Starting from $\Phi_N(x, y, z)$, we can obtain Newtonian acceleration $\boldsymbol{g}_N(x, y, z) = -\boldsymbol{\nabla}\Phi_N(x, y, z)$. Using the approximate relation between MOND acceleration and Newtonian acceleration $\boldsymbol{g}_M \approx \sqrt{a_0 g_N}\boldsymbol{g}_N/g_N$ (where $a_0 \approx 10^{-8}\mathrm{cms}^{-2}$ is the MOND critical acceleration), we obtain $\boldsymbol{g}_M$. Details on this approximation are given in Chapter 2.

(3) Using $\boldsymbol{g}_M(x, y, z)$, we calculate the second-order partial derivatives of the

lensing potential $\psi_M(x,y)$ in MOND. The lensing potential is defined as

$$\psi_M(x,y) = \frac{2D_{ls}}{D_l D_s c^2} \int_{-\infty}^{+\infty} \Phi_M(x,y,z), dz \tag{4.4}$$

where Φ_M is the MOND gravitational potential. Notice that we already know the first-order derivatives of Φ_M, i.e. $\boldsymbol{g}_M = -\boldsymbol{\nabla}\Phi_M(x,y,z) = -(\frac{\partial\Phi_M}{\partial x}, \frac{\partial\Phi_M}{\partial y}, \frac{\partial\Phi_M}{\partial z})$, so we can calculate the first-order partial derivative as:

$$\frac{\partial\psi_M(x,y)}{\partial x} = \frac{\partial}{\partial x}\int_{-\infty}^{+\infty}\Phi_M(x,y,z)dz = \int_{-\infty}^{+\infty}\frac{\partial\Phi_M(x,y,z)}{\partial x}dz = \int_{-\infty}^{+\infty} g_{Mx}(x,y,z)dz \tag{4.5}$$

and the second-order partial derivative as:

$$\frac{\partial^2\psi_M(x,y)}{\partial^2 x} = \frac{\partial}{\partial x}(\frac{\partial\psi_M(x,y)}{\partial x}) = \frac{\partial}{\partial x}\int_{-\infty}^{+\infty} g_{Mx}(x,y,z)dz = \int_{-\infty}^{+\infty}\frac{\partial g_{Mx}(x,y,z)}{\partial x}dz \tag{4.6}$$

Similarly, we can calculate $\frac{\partial^2\psi_M(x,y)}{\partial^2 y}$, $\frac{\partial^2\psi_M(x,y)}{\partial x\partial y}$ and $\frac{\partial^2\psi_M(x,y)}{\partial y\partial x}$.

(4) For each point on the lens plane (x,y), we calculate the shear component by

$$\begin{aligned}\gamma_1(x,y) &= \frac{1}{2}(\frac{\partial^2\psi_M(x,y)}{\partial^2 x} - \frac{\partial^2\psi_M(x,y)}{\partial^2 y}) \ , \\ \gamma_2(x,y) &= \frac{1}{2}(\frac{\partial^2\psi_M(x,y)}{\partial x\partial y} + \frac{\partial^2\psi_M(x,y)}{\partial y\partial x}) \ ,\end{aligned} \tag{4.7}$$

and finally obtain the shear $\gamma = \sqrt{\gamma_1^2 + \gamma_2^2}$.

The elliptical mass distribution lacks high symmetry, therefore the rigorous calculation of the MOND acceleration has to involve an extra curl term (see Chapter 2). To simplify this calculation, we use an approximation ($\boldsymbol{g}_M \approx \sqrt{a_0 g_N}\boldsymbol{g}_N/g_N$) for the exact MOND acceleration. Consequently, the resultant shear is an approximation to the exact shear in MOND. We note that the difference between the approximated MOND acceleration and the exact MOND acceleration decreases as $r^{-1.5}$ (as shown

in Chapter 2). After the series of integration and differentiation in steps (3) and (4), the difference between the approximated shear and the exact shear will decreases as fast as $r^{-2.5}$. We know that the shear in MOND for a point mass model decreases as r^{-1} (e.g., Chapter 3), which can be an estimate of the magnitude of the shear in MOND for our model on large radii. Therefore, our results on large scales are a reliable approximations to the rigorous solutions.

Given the mass of the galaxy in our model, we can calculate the shear in MOND at any external point. By comparing shears along different orientations, we can obtain the anisotropy in the tangential shear for this model in MOND. Since the extent and the ellipticity of the mass distribution are larger than the visible mass distribution in a galaxy, the anisotropic level of the shear from this model gives a upper limit of that induced by visible mass of a galaxy in MOND. In our study, we use this upper limit to compare with the real observed data. In the following, we first describe the data used for our comparison.

4.3 Observational Data

Parker et al. (2007) detected a significantly anisotropic galaxy-galaxy (g-g) lensing signal in a $\sim 22\ deg^2$ area of sky from the Canada-France-Hawaii Telescope Legacy Survey (CFHTLS). The data for analysis comes from the i' band only. Because these data lack color and redshift information for the lenses and the sources, the sample of lenses and sources is selected based on their apparent i' magnitude. Parker et al. (2007) define lens galaxies with $19 < i' < 22$ and source galaxies with $22.5 < i' < 24.5$. This selection yields $\sim 2 \times 10^5$ lenses and $\sim 1.3 \times 10^6$ sources. At the median redshift of the lenses, the angular scale of $7'' - 2'$ corresponds to a physical scale of $\sim 25 - 500h^{-1}$kpc. The source density is ~ 20 galaxies $arcmin^{-2}$. For more details on the data, we refer to Parker et al. (2007) and Hoekstra et al. (2006).

To measure the anisotropy in the g-g lensing signal, Parker et al. (2007) divided

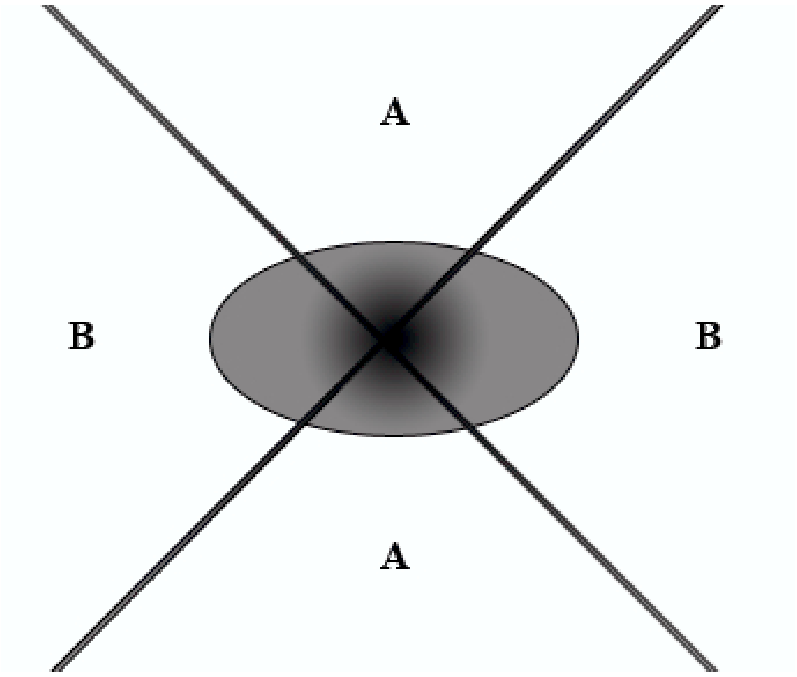

Figure 4.1: The sources are divided by Parker et al. (2007) into those within 45° of the semiminor axis of the lens galaxies (labeled with an 'A' region) and those within 45° of the semimajor axis (labeled with an 'B' region). From Fig. 7 in Parker et al. (2007).

the sources into those within 45° of the major axes and those within 45° of the minor axes of the lens galaxies. They measured the separate shears in those two different regions. $< \gamma >_{minor}$ is the mean shear in the 'A' regions and $< \gamma >_{major}$ is the mean shear in the 'B' regions (see the schematic in Fig. 4.1). They found the shears from these two regions are different. The shear ratio, $< \gamma >_{minor} / < \gamma >_{major}$, has an average value 0.76 ± 0.10 out to $70''$, which corresponds to $\sim 250h^{-1}$ kpc. Their measurement is presented in Fig. 4.2.

4.4 Comparison of Observations and Results

In order to compare to the observations, the mass of the galaxy in our model is set to $7.9 \times 10^{10} M_{\odot}$. From Chapter 3, we know that a point mass in MOND predicts a tangential shear profile that mimics that of an SIS model in the Newtonian framework. For a point mass of $7.9 \times 10^{10} M_{\odot}$ in MOND, it produces a lensing signal corresponding to a velocity dispersion of $\sigma_v \approx 135$ km/s in the SIS model. Parker et al. (2007) found

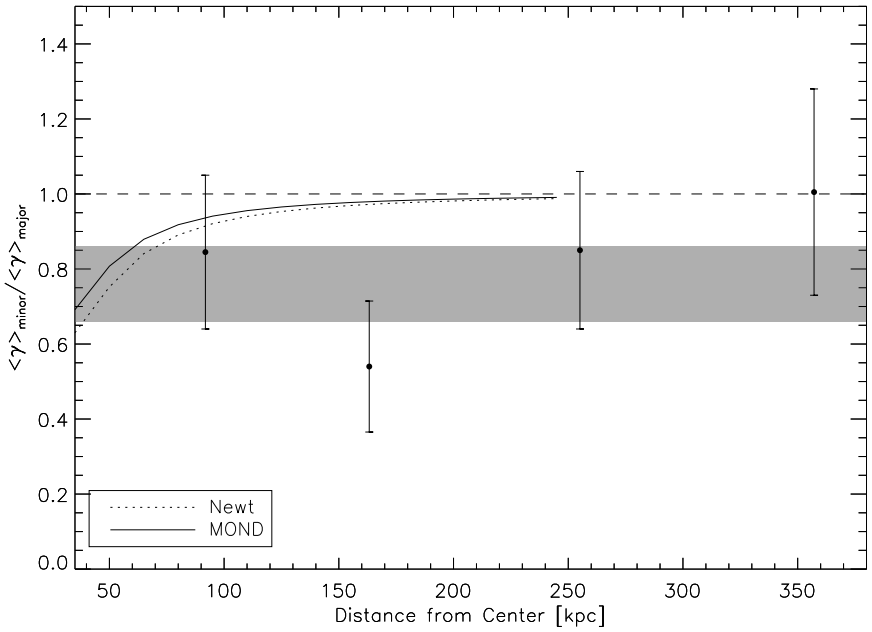

Figure 4.2: The data points are the ratios of mean shear obtained in Parker et al. (2007). $< \gamma >_{minor}$ is the mean shear in 'A' region and $< \gamma >_{major}$ is the mean shear in 'B' region. 'A', 'B' regions correspond to Fig. 4.1. The shadowed bar is the weighted average ratio 0.76 ± 0.10 of the data. The lines are our calculation for an ellipsoidal mass distribution. The mass model has an uniform density and a geometrical distribution of $a = c = 30$ kpc, $b = 3$ kpc. The total mass is $7.9 \times 10^{10} M_{\odot}$, which in MOND produces comparable weak lensing signals to Parker et al. (2007). The dotted line is the result for Newtonian gravity and the solid line is the result for MOND. The plots show that the shear ratio in MOND drops faster than that in the Newtonian case. Compared with the observations, MOND cannot reproduce such an extensive anisotropic shear given this mass distribution.

the best-fit velocity dispersion is 138 ± 15 km/s for the mean shear within 45° of the major axes (B regions); and the best-fit velocity dispersion is 122 ± 12 km/s for the mean shear within 45° of the minor axes (A regions). The mean velocity dispersion is therefore $\sigma_v = 135$ km/s. Hence, a galaxy of $7.9 \times 10^{10} M_{\odot}$ can produce a comparable magnitude of lensing signals in MOND as observed in Parker et al. (2007).

For comparison, we calculate the same shear ratio, $< \gamma >_{minor} / < \gamma >_{major}$. Fig. 4.2 presents our calculation results. The solid line is the result for MOND and the dotted line is the result for Newtonian gravity. Although our calculation only goes out to 250 kpc, we see the curves are asymptotic to 1 beyond this radius.

From Fig. 4.2, we can make the following two important points:

(1) With the same elliptical mass distribution, the ratio of azimuthal shear in MOND (the solid line) approaches unity faster than that in the Newtonian case (the dotted line). This result suggests that for a non-spherical mass distribution, the shear field in MOND is rounder than that in Newtonian gravity.

(2) Even with such an extremely high ellipticity (the ratio of the shortest to longest axes of the mass distribution = 0.1), a mass distribution of this extension cannot reproduce the extensive anisotropic shear in MOND that is observed. The shear ratios in Parker et al. (2007) have an average value 0.76 ± 0.10 out to a radius of $250h^{-1}$kpc. However, the shear ratio in MOND is already larger than 0.86 at 80 kpc, and the ratio quickly reaches 0.95 at 150 kpc. From this plot, we see the observed extensive anisotropic shear field can not be achieved from this mass distribution in MOND.

Compared with the real visible mass distribution in a galaxy, the mass extent and ellipticity in our model is an extreme case. Thus the anisotropy in the shear induced by real visible mass should be lower than that in our model. Therefore, it can be inferred that it is difficult for MOND to reproduce the observed anisotropic lensing signal from only the visible mass distribution.

In contrast, using an extensive elliptical dark matter halo to explain the observations, Parker et al. (2007) concluded that the fitted ellipticity of the halo is consistent with the prediction of ΛCDM simulations.

4.5 Discussion

In real data, lens galaxies are not isolated. The environment of a galaxy can contribute to the lensing signal around it. There are two main environmental factors which may affect the anisotropic lensing signals: neighboring galaxies or satellite galaxies and the external gravitational field. In the following, we discuss them sepa-

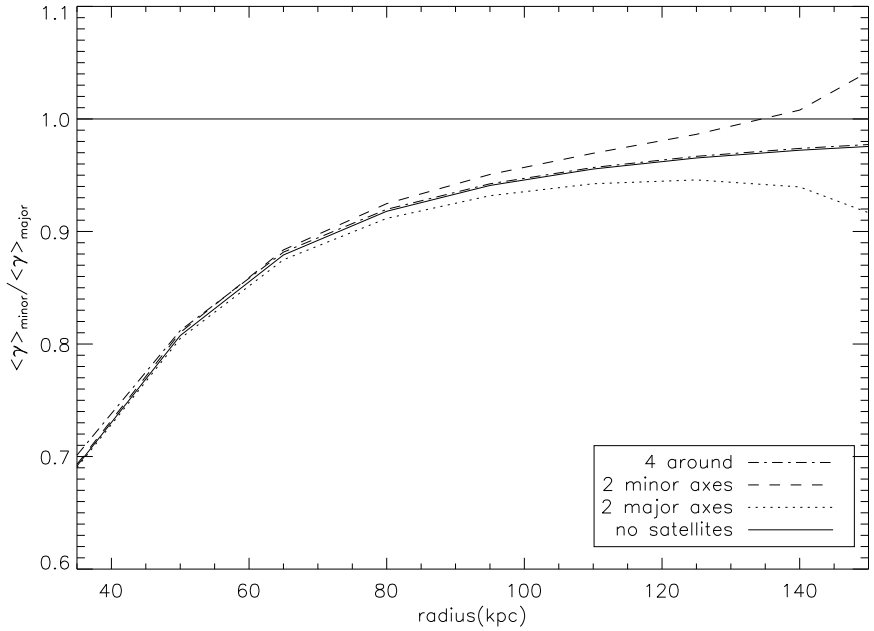

Figure 4.3: Investigating the effect of neighboring galaxies on the anisotropy of the lensing signal induced by the elliptical galaxy. The neighboring galaxies are at a distance of 200 kpc from the center galaxy. Note: the scale of the y-axis is different from that in Fig. 4.2.

rately.

4.5.1 Neighboring Galaxies

It is well known that most galaxies are found in groups or clusters. We need therefore to consider the contribution from neighboring galaxies to the lensing signal. It is expected that an anisotropic distribution of surrounding galaxies changes the anisotropy of the shear field. We investigate this effect by examining three simple situations. The first situation is to locate two neighboring galaxies on each side of major axis (x-axis). The second situation is to locate them on each side of the minor axis (y-axis). The third situation is to locate four neighboring galaxies each sides of both major and minor axes. Each neighbor has the same separation from the centre galaxies, 200 kpc. If neighboring galaxies are located further out, their effect will be smaller. And the situation for smaller separations are rare. In the first two distributions, each neighboring galaxy has half the mass of the center galaxy. In the third

case, each of the four neighboring galaxies has a quarter of the mass of the center galaxy. All the neighboring galaxies are modeled as point masses. The central galaxy has a mass distribution as before, i.e. an homogenous ellipsoid with $a = c = 30$ kpc, $b = 3$ kpc. Its total mass is $7.9 \times 10^{10} M_{\odot}$.

We calculate the same shear ratios around the center galaxy in MOND for these three situations. The results are presented in Fig. 4.3. From this plot, we see that when the neighboring galaxies are aligned with the major axis of the center galaxy, their presence increases the level of anisotropy of the lensing signal (the dotted line). When the surrounding galaxies are aligned with the minor axis of the center galaxy, their existence can decrease the level of anisotropic lensing signals (the dashed line). Finally, when the surrounding galaxies are distributed isotropically around the center galaxy, the anisotropic signal is not affected significantly (the dotted-dashed line). The solid line is the result with no neighboring galaxies.

4.5.2 Satellites Galaxies

For bright galaxies, the most significant effect comes from their satellite galaxies. Analysis of this situation is particularly important for our study because most lens galaxies in Parker et al. (2007) are bright galaxies. A recent simulation (Agustsson and Brainerd 2006) and the analysis of the galaxies in the SDSS (Brainerd 2005; Yang et al. 2006) indicate that satellite galaxies tend to be aligned along the major axis of the host galaxy. To investigate the effects from satellites, we assume two satellites located on each side of the major axis of the host galaxy. They are 50 kpc away from the host galaxy and each has a mass of 10% of the host galaxy. We also consider another situation in which the separation between the satellite and the host galaxy is 400 kpc. The analysis indicates close satellites help increase the anisotropic lensing signal on small scales, but they do not have a significant effect on the large scale (> 100 kpc). Far satellites have no effect on the anisotropic lensing signal within 200 kpc. The results are presented in Fig. 4.4. The dotted line is the result for the

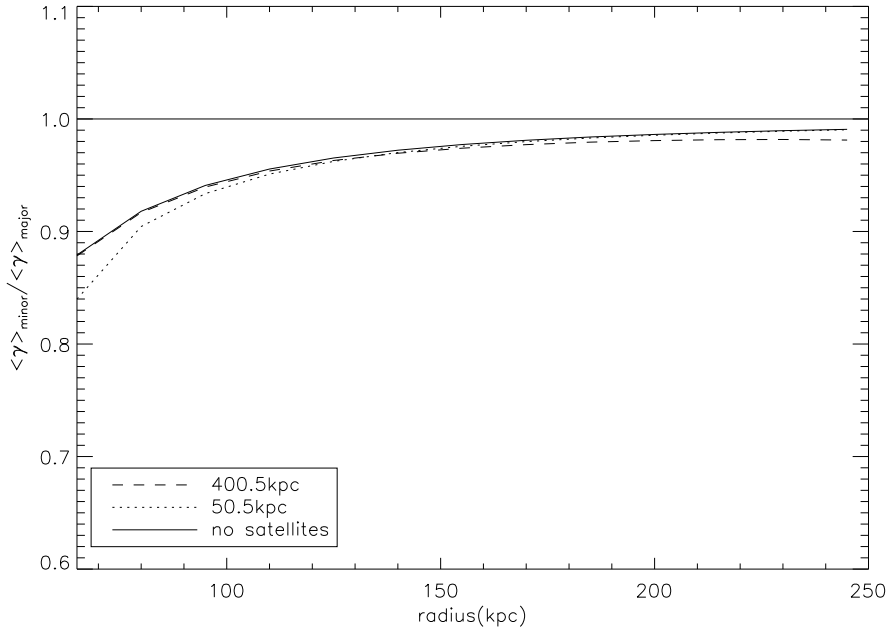

Figure 4.4: Investigating the effect of satellite galaxies on the anisotropy of the lensing signal induced by the elliptical galaxy.

separation of 50 kpc. The dashed line is the result for the separation of 400 kpc. The solid line is the case for no satellites.

Although we saw in §4.5.1 that the anisotropy level of the lensing signal can be increased by the surrounding galaxies when they are aligned with the major axis of the galaxy, because in our situation most surrounding galaxies are satellite galaxies, they do not help significantly.

4.5.3 External Field and Gas Halo

Another effect on the lensing signal is from external gravitational fields, which can be provided by filaments. In the Newtonian case, the contribution to the weak lensing signal from filaments is negligible (Dolag et al. 2006). In MOND, the contribution cannot be neglected (Feix et al. 2007). The results in Feix et al. (2007), however, are given for the filament which has a specific orientation. For a general case in which the filaments have random orientations with respect to the lens galaxies, the contribution

to the lensing signal is not clear. Even if the contribution from the filaments is not negligible, this only affects our results on the largest scales. More work is needed to fully quantify this.

Like galaxy clusters, elliptical galaxies are found surrounded by hot, ionized gas. This gas is observed in X-ray emission and is much more extended than the stellar mass (Humphrey et al. 2006). Adding a gas halo in our model complicates our analysis significantly. We leave it for future work. Because not all of elliptical galaxies have a gas halo, the work presented here without incorporating gas halos is still of value.

4.6 Conclusions

We study the anisotropic galaxy-galaxy (g-g) lensing signal induced by an elliptical mass distribution in MOND. According to MOND, only the visible mass is needed to account for all the observations. When a significantly anisotropic g-g lensing signal is observed over large radii, the relatively compact visible mass distribution should account for it.

Parker et al. (2007) detected an extensive anisotropic g-g lensing signal from the Canada-France-Hawaii Telescope Legacy Survey. In their measurement, the shear ratio $< \gamma >_{minor} / < \gamma >_{major}$ has an average value 0.76 ± 0.1 out to $\sim 250h^{-1}$ kpc. We attempt to reproduce such an extended anisotropic lensing signal in MOND with an extremely flattened mass distribution. We find it is difficult for MOND to reproduce such high anisotropic shear over large scales from our model. Because the real visible mass distributions are much rounder than our model, the corresponding anisotropy of the shear induced by them in MOND must be lower than that for our model.

We discuss the environmental effects from neighboring galaxies. We find, in our case, the existence of neighboring galaxies (satellites) does not help increase the anisotropy of the shear on large scales, although it does on small scales.

We note that we do not consider the effects from a gas halo and the external gravitation field. Unless they would significantly increase the anisotropy of the lensing signal (shear), it is very hard for MOND to reproduce an extensive anisotropic lensing signal from a relatively compact visible mass distribution. Also, although we focus on MOND in this work, our results are relevant for any alternative theory of gravity theories. Such theories all need to explain the observed extensive anisotropic g-g lensing signal from the compact visible mass distribution. Finally, we note that the g-g lensing measurements in Parker et al. (2007) use only a small fraction (1/8) of the total CFHTLS area ($\sim 170\ deg^2$). With more data coming in, the errors in the measurements will be greatly reduced and they will provide better constraints on alternative theories of gravity.

Chapter 5

Conclusions

We use galaxy-galaxy (g-g) lensing to compare MOND and cold dark matter, which are both proposed to explain observed discrepancies between luminous matter and the Newtonian gravitational mass. Previous work based on dynamical measurements claims MOND works very well on galactic scales. However, these studies are limited to the gravitational potential in inner regions of a galaxy. It is unclear how well MOND works in outer regions of galaxies. The outer regions are very important because they are where MOND and ΛCDM differ most markedly. The galaxy-galaxy lensing signal can be measured out to hundreds of kiloparsecs from the centers of galaxies, where direct dynamical methods fail. As such, we attempt to examine MOND in outer regions of galaxies with some of the latest g-g lensing data.

In Chapter 3, we study the amplitude of the weak gravitational lensing signal as a function of stellar mass around a sample of relatively isolated galaxies. This selection of lenses simplifies the interpretation of the observations, which consist of data from the Red-sequence Cluster Survey and the Sloan Digital Sky Survey. We find that the amplitude of the lensing signal as a function of stellar mass is well described by a power law with a best fit slope $\alpha = 0.74 \pm 0.08$. This result is inconsistent with Modified Newtonian Dynamics, which predicts $\alpha = 0.5$. (We find $\alpha > 0.5$ with 99.7% confidence). As a related test, we determine the MOND mass-to-light ratio

as a function of luminosity. Our results require dark matter for the most luminous galaxies ($L \sim 10^{11} L_{\odot}$). We rule out an extended halo of gas or neutrinos as a way of reconciling our findings with MOND.

In Chapter 4, we examine whether MOND can reproduce the observed anisotropic lensing signal around galaxies. The observational data in our study comes from the Canada-France-Hawaii Telescope Legacy Survey (CFHTLS). With the i' band imaging in a $\sim 22\ deg^2$ area of sky, Parker et al. (2007) detected that the ratio of mean shear along the minor axis to along the major axis, $< \gamma >_{minor} / < \gamma >_{major}$, has an average value of 0.76 ± 0.1 out to $\sim 250 h^{-1}$ kpc. We consider a mass distribution of extremely high ellipticity to represent visible mass distribution in a galaxy. The mass of the galaxy is chosen to reproduce the observed magnitude of lensing signals in Parker et al. (2007). We find the shear ratio in MOND rapidly converges to unity. Since the real visible mass distribution in a galaxy is rounder than our model, we infer it is very hard for MOND to reproduce the observed extensive anisotropic lensing signal from the compact visible mass.

These two tests demonstrate that MOND does not work well in the outer regions of galaxies. Given our results presented here, it seems doubtful MOND can convincingly prove itself as a viable alternative to dark matter. Although we focus on a single alternative gravity model, we note that our results are relevant for any alternative theory of gravity. Such theories not only need to explain dynamical properties of galaxies on small scales (e.g., rotation curves, the Tully-Fisher relation), but also need to explain observations of galaxies on large scales, like g-g lensing measurements.

Finally we note that much larger surveys, such as the extended CFHTLS, will significantly improve the data in coming years. Since the measurements in Parker et al. (2007) only use a small fraction of the total CFHTLS area, we can expect that with more data coming in, the g-g measurements will provide better constraints on alternative theories of gravity.

Bibliography

Agustsson, I. and Brainerd, T. G.: 2006, *ApJ* **650**, 550

Allgood, B., Flores, R. A., Primack, J. R., Kravtsov, A. V., Wechsler, R. H., Faltenbacher, A., and Bullock, J. S.: 2006, *MNRAS* **367**, 1781

Alonso, M. V., Valotto, C., Lambas, D. G., and Muriel, H.: 1999, *MNRAS* **308**, 618

Amendt, P. and Cuddeford, P.: 1994, *ApJ* **435**, 93

Angus, G. W.: 2008, *ArXiv e-prints* 804

Angus, G. W., Shan, H. Y., Zhao, H. S., and Famaey, B.: 2007, *ApJ* **654**, L13

Bahcall, N. A., Cen, R., Davé, R., Ostriker, J. P., and Yu, Q.: 2000, *ApJ* **541**, 1

Bartelmann, M. and Schneider, P.: 2001, *Phys. Rep.* **340**, 291

Baumgardt, H., Grebel, E. K., and Kroupa, P.: 2005, *MNRAS* **359**, L1

Bekenstein, J. and Milgrom, M.: 1984, *ApJ* **286**, 7

Bekenstein, J. D.: 2004, *Phys. Rev. D* **70(8)**, 083509

Bell, E. F. and de Jong, R. S.: 2001, *ApJ* **550**, 212

Bergmann, A. G., Petrosian, V., and Lynds, R.: 1990, *ApJ* **350**, 23

Binney, J. and Tremaine, S.: 1987, *Galactic dynamics*, Princeton, NJ, Princeton University Press, 1987, 747 p.

Blindert, K., Yee, H. K. C., Gladders, M. D., and Ellingson, E.: 2004, in A. Diaferio (ed.), *IAU Colloq. 195: Outskirts of Galaxy Clusters: Intense Life in the Suburbs*, pp 215–219

Brainerd, T. G.: 2005, *ApJ* **628**, L101

Bullock, J. S., Kolatt, T. S., Sigad, Y., Somerville, R. S., Kravtsov, A. V., Klypin, A. A., Primack, J. R., and Dekel, A.: 2001, *MNRAS* **321**, 559

Buote, D. A. and Canizares, C. R.: 1996, *ApJ* **457**, 177

Buote, D. A. and Canizares, C. R.: 1997, *ApJ* **474**, 650

Buote, D. A. and Canizares, C. R.: 1998, *MNRAS* **298**, 811

Carroll, B. W. and Ostlie, D. A.: 1996, *An introduction to modern astrophysics*, Reading, MA: Addison-Wesley, —c1996

Chandrasekhar, S.: 1969, *Ellipsoidal figures of equilibrium*, The Silliman Foundation Lectures, New Haven: Yale University Press, 1969

Chen, D.-M. and Zhao, H.: 2006, *ApJ* **650**, L9

Conroy, C., Prada, F., Newman, J. A., Croton, D., Coil, A. L., Conselice, C. J., Cooper, M. C., Davis, M., Faber, S. M., Gerke, B. F., Guhathakurta, P., Klypin, A., Koo, D. C., and Yan, R.: 2007, *ApJ* **654**, 153

Corbelli, E. and Salucci, P.: 2007, *MNRAS* **374**, 1051

Dolag, K., Meneghetti, M., Moscardini, L., Rasia, E., and Bonaldi, A.: 2006, *MNRAS* **370**, 656

Dubinski, J.: 1994, *ApJ* **431**, 617

Dubinski, J. and Carlberg, R. G.: 1991, *ApJ* **378**, 496

Dubinski, J. and Kuijken, K.: 1995, *ApJ* **442**, 492

Fahlman, G., Kaiser, N., Squires, G., and Woods, D.: 1994, *ApJ* **437**, 56

Famaey, B. and Binney, J.: 2005, *MNRAS* **363**, 603

Feix, M., Xu, D., Shan, H., Famaey, B., Limousin, M., Zhao, H., and Taylor, A.: 2007, *ArXiv e-prints* 710

Ferreras, I., Sakellariadou, M., and Yusaf, M. F.: 2008, *Physical Review Letters* **100(3)**, 031302

Fischer, P., McKay, T. A., Sheldon, E., Connolly, A., Stebbins, A., Frieman, J. A., Jain, B., Joffre, M., Johnston, D., Bernstein, G., Annis, J., Bahcall, N. A., Brinkmann, J., Carr, M. A., Csabai, I., Gunn, J. E., Hennessy, G. S., Hindsley, R. B., Hull, C., Ivezić, Ž., Knapp, G. R., Limmongkol, S., Lupton, R. H., Munn, J. A., Nash, T., Newberg, H. J., Owen, R., Pier, J. R., Rockosi, C. M., Schneider, D. P., Smith, J. A., Stoughton, C., Szalay, A. S., Szokoly, G. P., Thakar, A. R., Vogeley, M. S., Waddell, P., Weinberg, D. H., York, D. G., and The SDSS Collaboration: 2000, *AJ* **120**, 1198

Frenk, C. S., White, S. D. M., Davis, M., and Efstathiou, G.: 1988, *ApJ* **327**, 507

Gentile, G., Famaey, B., Combes, F., Kroupa, P., Zhao, H. S., and Tiret, O.: 2007, *A&A* **472**, L25

Gladders, M. D. and Yee, H. K. C.: 2005, *ApJS* **157**, 1

Goto, T.: 2005, *MNRAS* **359**, 1415

Grossman, S. A. and Narayan, R.: 1989, *ApJ* **344**, 637

Hoekstra, H., Hsieh, B. C., Yee, H. K. C., Lin, H., and Gladders, M. D.: 2005, *ApJ* **635**, 73

Hoekstra, H. and Jain, B.: 2008, *ArXiv e-prints* 805

Hoekstra, H., Mellier, Y., van Waerbeke, L., Semboloni, E., Fu, L., Hudson, M. J., Parker, L. C., Tereno, I., and Benabed, K.: 2006, *ApJ* **647**, 116

Hoekstra, H., Yee, H. K. C., and Gladders, M. D.: 2004, *ApJ* **606**, 67

Humphrey, P. J., Buote, D. A., Gastaldello, F., Zappacosta, L., Bullock, J. S., Brighenti, F., and Mathews, W. G.: 2006, *ApJ* **646**, 899

Kahn, F. D. and Woltjer, L.: 1959, *ApJ* **130**, 705

Kaiser, N.: 1995, *ApJ* **439**, L1

Kaiser, N. and Squires, G.: 1993, *ApJ* **404**, 441

Katz, N. and Gunn, J. E.: 1991, *ApJ* **377**, 365

Kauffmann, G., Heckman, T. M., White, S. D. M., Charlot, S., Tremonti, C., Brinchmann, J., Bruzual, G., Peng, E. W., Seibert, M., Bernardi, M., Blanton, M., Brinkmann, J., Castander, F., Csábai, I., Fukugita, M., Ivezic, Z., Munn, J. A., Nichol, R. C., Padmanabhan, N., Thakar, A. R., Weinberg, D. H., and York, D.: 2003, *MNRAS* **341**, 33

Kneib, J. P., Mellier, Y., Fort, B., and Mathez, G.: 1993, *A&A* **273**, 367

Lewis, A. D., Buote, D. A., and Stocke, J. T.: 2003, *ApJ* **586**, 135

Luppino, G. A. and Kaiser, N.: 1997, *ApJ* **475**, 20

Mandelbaum, R., Hirata, C. M., Broderick, T., Seljak, U., and Brinkmann, J.: 2006a, *MNRAS* **370**, 1008

Mandelbaum, R., Seljak, U., Kauffmann, G., Hirata, C. M., and Brinkmann, J.: 2006b, *MNRAS* **368**, 715

McKay, T. A., Sheldon, E. S., Johnston, D., Grebel, E. K., Prada, F., Rix, H.-W., Bahcall, N. A., Brinkmann, J., Csabai, I., Fukugita, M., Lamb, D. Q., and York, D. G.: 2002, *ApJ* **571**, L85

Mellier, Y., Fort, B., and Kneib, J.-P.: 1993, *ApJ* **407**, 33

Milgrom, M.: 1983a, *ApJ* **270**, 371

Milgrom, M.: 1983b, *ApJ* **270**, 365

Milgrom, M.: 2001, *MNRAS* **326**, 1261

Moore, B., Quinn, T., Governato, F., Stadel, J., and Lake, G.: 1999, *MNRAS* **310**, 1147

Mortlock, D. J. and Turner, E. L.: 2001a, *MNRAS* **327**, 552

Mortlock, D. J. and Turner, E. L.: 2001b, *MNRAS* **327**, 557

Narayan, R. and Bartelmann, M.: 1996, *ArXiv Astrophysics e-prints*

Navarro, J. F., Frenk, C. S., and White, S. D. M.: 1996, *ApJ* **462**, 563

Nipoti, C., Londrillo, P., Zhao, H., and Ciotti, L.: 2007, *MNRAS* **379**, 597

Ostriker, J. P. and Peebles, P. J. E.: 1973, *ApJ* **186**, 467

Parker, L. C., Hoekstra, H., Hudson, M. J., van Waerbeke, L., and Mellier, Y.: 2007, *ApJ* **669**, 21

Pello, R., Sanahuja, B., Le Borgne, J.-F., Soucail, G., and Mellier, Y.: 1991, *ApJ* **366**, 405

Pointecouteau, E. and Silk, J.: 2005, *MNRAS* **364**, 654

Prada, F., Vitvitska, M., Klypin, A., Holtzman, J. A., Schlegel, D. J., Grebel, E. K., Rix, H.-W., Brinkmann, J., McKay, T. A., and Csabai, I.: 2003, *ApJ* **598**, 260

Read, J. I. and Moore, B.: 2005, *MNRAS* **361**, 971

Rubin, V. C., Burstein, D., Ford, Jr., W. K., and Thonnard, N.: 1985, *ApJ* **289**, 81

Rubin, V. C. and Ford, W. K. J.: 1970, *ApJ* **159**, 379

Ryden, B.: 2003, *Introduction to cosmology*, Introduction to cosmology / Barbara Ryden. San Francisco, CA, USA: Addison Wesley, ISBN 0-8053-8912-1, 2003, IX + 244 pp.

Sanders, R. H.: 2003, *MNRAS* **342**, 901

Sanders, R. H.: 2007, *MNRAS* **380**, 331

Sanders, R. H. and McGaugh, S. S.: 2002, *ARA&A* **40**, 263

Sarazin, C. L.: 1988, *X-ray emission from clusters of galaxies*, Cambridge Astrophysics Series, Cambridge: Cambridge University Press, 1988

Seitz, S. and Schneider, P.: 1996, *A&A* **305**, 383

Seljak, U.: 2000, *MNRAS* **318**, 203

Sellwood, J. A. and Kosowsky, A.: 2002, in G. S. Da Costa and H. Jerjen (eds.), *The Dynamics, Structure History of Galaxies: A Workshop in Honour of Professor Ken Freeman*, Vol. 273 of *Astronomical Society of the Pacific Conference Series*, pp 243–+

Skordis, C., Mota, D. F., Ferreira, P. G., and Bœhm, C.: 2006, *Physical Review Letters* **96(1)**, 011301

Smail, I., Ellis, R. S., Fitchett, M. J., and Edge, A. C.: 1995, *MNRAS* **273**, 277

Smith, S.: 1936, *ApJ* **83**, 23

Spergel, D. N., Bean, R., Doré, O., Nolta, M. R., Bennett, C. L., Dunkley, J., Hinshaw, G., Jarosik, N., Komatsu, E., Page, L., Peiris, H. V., Verde, L., Halpern, M., Hill, R. S., Kogut, A., Limon, M., Meyer, S. S., Odegard, N., Tucker, G. S., Weiland, J. L., Wollack, E., and Wright, E. L.: 2007, *ApJS* **170**, 377

Springel, V., White, S. D. M., and Hernquist, L.: 2004, in S. Ryder, D. Pisano, M. Walker, and K. Freeman (eds.), *Dark Matter in Galaxies*, Vol. 220 of *IAU Symposium*, pp 421–+

Squires, G., Kaiser, N., Fahlman, G., Babul, A., and Woods, D.: 1996, *ApJ* **469**, 73

Takahashi, R. and Chiba, T.: 2007, *ApJ* **671**, 45

Thomas, P. A., Colberg, J. M., Couchman, H. M. P., Efstathiou, G. P., Frenk, C. S., Jenkins, A. R., Nelson, A. H., Hutchings, R. M., Peacock, J. A., Pearce, F. R., and White, S. D. M.: 1998, *MNRAS* **296**, 1061

Tyson, J. A. and Fischer, P.: 1995, *ApJ* **446**, L55+

van den Bergh, S.: 1961, *AJ* **66**, 566

van der Marel, R. P.: 1991, *MNRAS* **253**, 710

Warren, M. S., Quinn, P. J., Salmon, J. K., and Zurek, W. H.: 1992, *ApJ* **399**, 405

Yang, X., van den Bosch, F. C., Mo, H. J., Mao, S., Kang, X., Weinmann, S. M., Guo, Y., and Jing, Y. P.: 2006, *MNRAS* **369**, 1293

York, D. G., Adelman, J., Anderson, Jr., J. E., Anderson, S. F., Annis, J., Bahcall, N. A., Bakken, J. A., Barkhouser, R., Bastian, S., Berman, E., Boroski, W. N., Bracker, S., Briegel, C., Briggs, J. W., Brinkmann, J., Brunner, R., Burles, S., Carey, L., Carr, M. A., Castander, F. J., Chen, B., Colestock, P. L., Connolly,

A. J., Crocker, J. H., Csabai, I., Czarapata, P. C., Davis, J. E., Doi, M., Dombeck, T., Eisenstein, D., Ellman, N., Elms, B. R., Evans, M. L., Fan, X., Federwitz, G. R., Fiscelli, L., Friedman, S., Frieman, J. A., Fukugita, M., Gillespie, B., Gunn, J. E., Gurbani, V. K., de Haas, E., Haldeman, M., Harris, F. H., Hayes, J., Heckman, T. M., Hennessy, G. S., Hindsley, R. B., Holm, S., Holmgren, D. J., Huang, C.-h., Hull, C., Husby, D., Ichikawa, S.-I., Ichikawa, T., Ivezić, Ž., Kent, S., Kim, R. S. J., Kinney, E., Klaene, M., Kleinman, A. N., Kleinman, S., Knapp, G. R., Korienek, J., Kron, R. G., Kunszt, P. Z., Lamb, D. Q., Lee, B., Leger, R. F., Limmongkol, S., Lindenmeyer, C., Long, D. C., Loomis, C., Loveday, J., Lucinio, R., Lupton, R. H., MacKinnon, B., Mannery, E. J., Mantsch, P. M., Margon, B., McGehee, P., McKay, T. A., Meiksin, A., Merelli, A., Monet, D. G., Munn, J. A., Narayanan, V. K., Nash, T., Neilsen, E., Neswold, R., Newberg, H. J., Nichol, R. C., Nicinski, T., Nonino, M., Okada, N., Okamura, S., Ostriker, J. P., Owen, R., Pauls, A. G., Peoples, J., Peterson, R. L., Petravick, D., Pier, J. R., Pope, A., Pordes, R., Prosapio, A., Rechenmacher, R., Quinn, T. R., Richards, G. T., Richmond, M. W., Rivetta, C. H., Rockosi, C. M., Ruthmansdorfer, K., Sandford, D., Schlegel, D. J., Schneider, D. P., Sekiguchi, M., Sergey, G., Shimasaku, K., Siegmund, W. A., Smee, S., Smith, J. A., Snedden, S., Stone, R., Stoughton, C., Strauss, M. A., Stubbs, C., SubbaRao, M., Szalay, A. S., Szapudi, I., Szokoly, G. P., Thakar, A. R., Tremonti, C., Tucker, D. L., Uomoto, A., Vanden Berk, D., Vogeley, M. S., Waddell, P., Wang, S.-i., Watanabe, M., Weinberg, D. H., Yanny, B., and Yasuda, N.: 2000, *AJ* **120**, 1579

Zaritsky, D. and White, S. D. M.: 1994, *ApJ* **435**, 599

Zhao, H.: 2006, *ArXiv Astrophysics e-prints*

Zhao, H.: 2007, *ArXiv e-prints* 704

Zhao, H., Bacon, D. J., Taylor, A. N., and Horne, K.: 2006, *MNRAS* **368**, 171

Zhao, H. and Tian, L.: 2006, *A&A* **450**, 1005

Zhao, H. S.: 2005, *A&A* **444**, L25

Zhao, H. S. and Famaey, B.: 2006, *ApJ* **638**, L9

Zlosnik, T. G., Ferreira, P. G., and Starkman, G. D.: 2007, *Phys. Rev. D* **75(4)**, 044017

Zwicky, F.: 1937, *ApJ* **86**, 217

University of Victoria

Partial Copyright License

Title of Thesis: Distinguishing Modified Newtonian Dynamics from Dark Matter with Galaxy-galaxy Lensing Measurements.

Author: _____

Lanlan Tian

June 20, 2008